Secondary reactions of aromatics-derived oxygenated organic molecules lead to plentiful highly oxygenated organic molecules within an intraday OH exposure

Yuwei Wang[1], Yueyang Li[1], Gan Yang[1], Xueyan Yang[1], Yizhen Wu[1], Chuang Li[1], Lei Yao[1,2], Hefeng, Zhang[3*], Lin Wang[1,2,4,5,6] *

[1] Shanghai Key Laboratory of Atmospheric Particle Pollution and Prevention (LAP[3]), Department of Environmental Science and Engineering, Jiangwan Campus, Fudan University, Shanghai 200438, China

[2] Shanghai Institute of Pollution Control and Ecological Security, Shanghai 200092, China

[3] State Environmental Protection Key Laboratory of Vehicle Emission Control and Simulation, Vehicle Emission Control Center of Ministry of Ecology and Environment, Chinese Research Academy of Environmental Sciences, Beijing 100012, China

[4] IRDR International Center of Excellence on Risk Interconnectivity and Governance on Weather/Climate Extremes Impact and Public Health, Fudan University

[5] National Observations and Research Station for Wetland Ecosystems of the Yangtze Estuary, Shanghai, China

[6] Collaborative Innovation Center of Climate Change, Nanjing, 210023, China

Corresponding Author: H.Z., email, zhanghf@craes.org.cn; phone, +86-10-84915586
L.W., email, lin_wang@fudan.edu.cn; phone, +86-21-31243568

ABSTRACT. Highly oxygenated organic molecules (HOMs) can participate in new particle formation (NPF) and enhance growth of newly formed particles partially because of their low volatility. Previous studies have shown formation of HOMs via autoxidation reactions of RO_2 intermediates generated by OH-initiated oxidation of anthropogenic volatile organic compounds (VOCs). It was also suggested that multi-generation OH oxidation could be an important source for aromatics-derived HOMs. However, our understanding on the generation of aromatics-derived HOMs are still insufficient, especially for their formation mechanisms, which determine molar yields of HOMs and are essential to the establishment of global chemical box models related to HOMs. In this study, with a potential aerosol formation oxidation flow reactor (PAM OFR), a series of OH-initiated oxidation experiments of 1,3,5-trimethylbenzene (1,3,5-TMB) were conducted to investigate the influences of the extent of OH exposure on the formation of aromatics-derived HOMs. The evolution of oxidation products of 1,3,5-TMB in an OH exposure range of $(0.5 – 5.0) \times 10^{10}$ molecules cm^{-3} s, equivalent to an OH exposure of 0.7 – 6.9 hours at an OH concentration of 2×10^6 molecules cm^{-3}, was investigated by a nitrate-based chemical ionization mass spectrometer and a Vocus proton-transfer-reaction mass spectrometer, indicating significant secondary OH chemistry

37 during the ageing of stabilized first generation oxygenated products within an intraday OH

38 exposure and formation of various HOMs with more oxygen content and thus lower volatility.

39 In addition, organonitrates, formed after the introduction of NO_x into the reaction systems,

40 further confirmed the existence of such secondary reactions. Our study suggests an important

41 role of secondary OH chemistry in the oxidation of aromatics and elucidates detailed formation

42 mechanisms of certain HOM products.

44 **1 Introduction**

45   OH radicals can react with volatile organic compounds (VOCs) in the atmosphere,

46 converting primary pollutants to secondary ones. Generated from oxidation of VOCs,

47 oxygenated organic molecules (OOMs) are crucial in a variety of atmospheric chemical

48 processes, contributing efficiently to the formation of secondary organic aerosols (SOAs) and

49 ground-level O_3 (Ng et al., 2010; Wang et al., 2022; Qu et al., 2021). Among the enormous

50 number of oxygenated VOCs (OVOCs), highly oxygenated organic molecules (HOMs) have

51 recently attracted significant attention (Bianchi et al., 2019). Most of HOMs are low volatile

52 organic compounds (LVOCs) or extremely low volatile organic compounds (ELVOCs), and

53 thus are able to drive the initial formation of nucleated particles under certain conditions and

54 contribute to the subsequent growth of newly-formed particles, which finally enhance SOA

55 formation (Tröstl et al., 2016; Lehtipalo et al., 2018; Stolzenburg et al., 2018; Mohr et al., 2019;

56 Qiao et al., 2021).

57   Formation of HOMs is typically triggered by oxidation of VOCs in the gas phase. Peroxy

58 radicals (RO_2) are generated at the initial step and will undergo an intramolecular hydrogen

59 atom shift forming a hydroperoxide functionality and an alkyl radical. A molecular oxygen will

60 rapidly attach to this alkyl radical and form a new and more oxidized RO_2. This reaction is

61 called as autoxidation and the newly formed RO_2 can go through another autoxidation or

62 bimolecular termination reactions to form a stabilized product (Crounse et al., 2013).

63 Autoxidation is suggested to be responsible for widely detected HOMs in the atmosphere,

64 because it can form highly oxygenated RO_2 in a short time scale. In terms of biomolecular

65 reactions, RO_2 reacts appreciable only with hydroperoxyl radical (HO_2), NO, and another RO_2.

66 The RO_2 reaction chain in polluted areas is largely terminated by NO, which prohibits

67 generation of compounds with high oxidation levels and reduces yields of HOMs (Bianchi et

68 al., 2019).

69   Nevertheless, autoxidation reactions alone are not enough to explain the large numbers of

70 oxygen atoms in HOMs observed in laboratory experiments and ambient campaigns. Take

71 alkylbenzenes as an example, previous studies suggest that the main products of OH-initiated

72 oxidation of alkylbenzenes (C_xH_{2x-6}, x=7, 8, or 9), i.e., bicyclic peroxy radicals (BPR, $C_xH_{2x-6}O_5^{\bullet}$, x=7, 8, or 9) (Jenkin et al., 2003), can undergo an autoxidation reaction and form a new peroxy radical, $C_xH_{2x-6}O_7^{\bullet}$ (x=7, 8, or 9) (Wang et al., 2017). ~~Take alkylbenzenes as an example, previous studies suggest that the main products of OH oxidation of alkylbenzenes (C_xH_{2x-6}, x=7, 8, or 9), i.e., bicyclic peroxy radicals (BPR, $C_xH_{2x-6}O_5^{\bullet}$, x=7, 8, or 9), can undergo an autoxidation reaction and form a new peroxy radical, $C_xH_{2x-6}O_7^{\bullet}$ (x=7, 8, or 9) (Jenkin et al., 2003).~~ The autoxidation of BPR could be fast if it has a favorable structure, as found in a previous study ~~The autoxidation reaction of BPR could be very fast because an allylic radical will be formed after the hydrogen shift~~ (Wang et al., 2017). On the other hand, the structure of resulting $C_xH_{2x-6}O_7^{\bullet}$ is strongly different from that of BPR, whose autoxidation reaction rate can be as low as the order of 0.001 s^{-1}, since it lacks enhancements from favorable transition state geometries and substitutes or resonance structures (Bianchi et al., 2019; Otkjær et al., 2018). Such a slow autoxidation reaction rate cannot explain the extensive existence of HOM monomers with more than 7 oxygen atoms and HOM dimers with more than 10 oxygen atoms, which are the maximum numbers of oxygen atoms in stabilized monomer and dimer products, respectively, formed from $C_xH_{2x-6}O_7^{\bullet}$ (Molteni et al., 2018; Wang et al., 2020; Mentel et al., 2015). Another possibility is the formation of a second oxygen bridge after the hydrogen shift of BPR (Molteni et al., 2018), but this reaction pathway would not allow a further oxygenation reaction without a breakage of the carbon ring, which is also unpromising. A very recent investigation offers new insights into the formation mechanism of these products, indicating the molecular rearrangement of BPR can initiate a series of autoxidation (Iyer et al., 2023). However, the formation mechanism of HOMs with a large hydrogen atom number is still vague, e.g., monomer products with 16 hydrogen atoms in the OH-initiated oxidation of TMB and with 14 hydrogen atoms in the OH-initiated oxidation of xylene.

Multigeneration reactions of VOCs complicate HOMs' formation. Previous studies indicate that HOMs can also be formed by sequential oxidation of stabilized first-generation products of benzene and toluene (Garmash et al., 2020; Cheng et al., 2021). Garmash et al. (2020) conducted OH oxidation experiments of benzene and toluene with an OH exposure equivalent to atmospheric oxidation times of 10 hours – 15 days at OH concentrations of ~10^6 molecules cm^{-3}. Cheng et al. (2021) simulated oxidation of benzene and toluene with an OH exposure equivalent to 2.4 – 19.4 days of atmospheric photochemical ageing. Certainly, such extremely high OH exposures favor secondary OH chemistry and help to facilitate our understanding on product distributions, but such a long timescale limits atmospheric implications of their results, given the complex physical and chemical processes at night.

106   Compared to benzene and toluene, trimethylbenzene (TMB) is a precursor characterized

107   with much larger HOM molar yields when reacted with OH, and the abundance of TMB in the

108   atmosphere is unignorable (Molteni et al., 2018; Yuan et al., 2012). Previous laboratory

109   experiments on TMB-derived HOMs mainly focused on the autoxidation reactions of BPR and

110   the influences of NO_x, while the quantity of experiments was finite with a limited range of OH

111   exposure, bringing down the universality and applicability of conclusions (Tsiligiannis et al.,

112   2019; Wang et al., 2020). From the mechanism perspective, a number of HOM monomers with

113   more than 7 oxygen atoms detected in the OH-initiated oxidation of TMB were previously

114   assumed to be generated via multiple autoxidation reactions (Molteni et al., 2018). Nevertheless,

115   a subsequent OH oxidation of the first-generation oxygenated products might be more plausible

116   for the formation of HOM monomers with more than 7 oxygen atoms from the present point of

117   view. Indeed, laboratory experiments show that RO_2 formed during the second-generation OH

118   oxidation of the first-generation stabilized oxidation products can also undergo autoxidation

119   reactions, which entangles reaction mechanisms potentially involved in the formation of those

120   HOMs and justifies more investigations on the multigeneration OH oxidation of aromatics

121   (Wang et al., 2020). OH with an atmospheric concentration up to 6×10^6 – 2.6×10^7 molecule

122   cm^{-3}, which is several times higher than the typical average atmospheric OH concentration,

123   1.5×10^6 molecule cm^{-3} (Jacob, 1999), has been frequently observed in both urban and suburban

124   environments in China (Tan et al., 2019; Lu et al., 2012). High atmospheric concentrations of

125   OH have been frequently observed in both urban and suburban environments in China (Tan et

126   al., 2019; Lu et al., 2012), leading to a realistic implication of multigeneration OH oxidation.

127   Therefore, it is imperative to study chemical characteristics of formation reactions of HOMs at

128   different OH exposures, especially those fewer than or equivalent to one day of atmospheric

129   oxidation.

130   In this study, a series of laboratory experiments were conducted on the OH-initiated

131   oxidation of 1,3,5-TMB, selected as an example of anthropogenic VOCs with an OH exposure

132   equivalent to atmospheric oxidation times of roughly 0.7 – 6.9 hours at an average daytime OH

133   radical concentration of 2.0×10^6 molecules cm^{-3}. A nitrate-based chemical ionization mass

134   spectrometer (nitrate CIMS) and a Vocus proton-transfer-reaction mass spectrometer (Vocus

135   PTR) were deployed to measure the oxidation products and the precursor, respectively. From

136   the evolution of oxygenated products, we explored secondary OH chemistry of stabilized first-

137   generation oxygenated products generated by the oxidation of 1,3,5-TMB. Furthermore, the

138   influence of NO on the formation of HOMs was investigated by introducing N_2O into the

139   reaction system via formation of organonitrates.

140   **2 Methods**

OH-initiated oxidation of 1,3,5-TMB was investigated in a potential aerosol formation oxidation flow reactor (PAM OFR) system at $T = 298 \pm 1$ K and a pressure of 1 atm (Lambe et al., 2015). The experimental settings in this study differed slightly from what were used previously (Wang et al., 2020). Forty OH experiments (Exp. 1 – 40) and twenty-eight NO_x experiments (Exp. 41 – 68) were performed, the experimental conditions of which are summarized in Table S1, including concentrations of the precursor, ozone, and NO and NO_2. The equivalent OH exposure in the OFR for each experiment was estimated according to the precursor consumption, also listed in Table S1. OH exposures in the OFR were in the range of $(0.5 – 5.0) \times 10^{10}$ molecules cm^{-3} s, equivalent to atmospheric oxidation times of roughly 0.7 – 6.9 hours for 1,3,5-TMB at an average daytime OH radical concentration of 2.0×10^6 molecules cm^{-3}. In contrast, the OH oxidation lifetime for 1,3,5-TMB is around 2.4 hours at the aforementioned atmospheric average daytime OH concentrations.

A home-made 1,3,5-TMB/N_2 cylinder was used as a stable gaseous precursor source in the experiments, from which the flow rate of 1,3,5-TMB/N_2 varied between 1 – 3 sccm (standard cubic centimeter per minute, standard to 0 °C, 1 atm), leading to 28.9 – 62.7 ppb of 1,3,5-TMB in the OH oxidation experiments (Table S1). A total flow of 15 slpm (standard liters per minute, standard to 0 °C, 1 atm) zero-gas generated by a zero-gas generator (model 737-13, Aadco Instruments Inc.), together with the 1,3,5-TMB/N_2 flow, was introduced into the OFR. The reaction time in this series of experiments was kept at around 53 s. The flow in the PAM OFR is laminar with a very low axial mixing, as characterized with a Taylor dispersion model in a previous study (Lambe et al., 2011). Among the 15 slpm zero-gas, 6 slpm was initially passed through a Nafion humidifier (Perma Pure Model FC100-80-6MSS) filled with ultra-pure water and finally converged with the main flow into the OFR to achieve and keep a desired RH of 20.0 ± 2.5 % in the OFR throughout all the experiments, and 2 slpm was initially passed through a separate ozone chamber, resulting in an initial ozone concentration of around 429 – 881 ppb in the OFR. The OFR was operated with only the 254 nm lights on, under which the primary oxidant production reactions in the OFR were $O_3 + h\nu\ (254\ nm) \rightarrow O_2 + O(^1D)$ and $O(^1D) + H_2O \rightarrow 2OH$. After turning on of UV lights, a certain HOM compound is believed to be generated if its signal is more than 3 standard deviations of its background signal. If the fluctuations in the 1-min-averaged signals of both TMB in the Vocus PTR and typical HOMs (i.e., $C_9H_{14}O_7(NO_3)^-$) in the nitrate CIMS are within 2% during a 10-min period, we assume that a steady state has been reached. It usually took around no more than 2 minutes for the signals of HOMs to stabilize after the adjustment of UV lights. We typically monitored the reaction products for around 20 minutes for each experiment. An ozone monitor (Model 106-

175 M, 2B technologies) and a trace-gas analyzer for NO-NO_2-NO_x (Thermo, 42i-TL) were placed

176 at the exit of the OFR to measure concentrations of ozone and NO_x, respectively.

177   Non-tropospheric VOC photolysis is a typical issue that should be taken into account when

178 evaluating the settings of OFR laboratory experiments. Photolysis of the precursor and HOMs

179 were evaluated, showing that photolysis was not a contributor to our observation. The

180 photolysis rate of 1,3,5-TMB can be estimated based on the absorption cross-sections of 1,3,5-

181 TMB at 254 nm (Keller-Rudek et al., 2013) and UV photon fluxes estimated by a chemistry

182 model discussed in the following sections. The ratio of photolysis-to-OH reaction in our

183 experiments was merely 0.010 – 0.033. Hence, photolysis of 1,3,5-TMB was insignificant in

184 the OFR.

185   For stabilized products such as HOMs, the cross sections of organic molecules are usually

186 $\sim 3.9\times10^{-18}$ - 3.9×10^{-17} cm^2 (Peng et al., 2016), while the reaction rate between OH and the

187 stabilized first-generation products are estimated to be around 1.28×10^{-10} molecule^{-1} cm^3 s^{-1}, as

188 suggested by MCM (Jenkin et al., 2003). Hence, the ratio of photolysis rates of HOMs to their

189 secondary OH oxidation rates is estimated to be merely around 0.020 – 0.056.

190   For experiments with NO_x, 350 sccm N_2O (99.999%, Air Liquid) was added into the OFR

191 to produce and sustain NO_x mixing ratios at levels that were sufficiently high to be a competitive

192 sink for RO_2 radicals. NO and NO_2 were produced via the reaction $N_2O + O(^1D) \rightarrow 2NO$,

193 followed by the reaction $NO + O_3 \rightarrow NO_2 + O_2$. Two sets of irradiance intensities were chosen

194 for NO_x experiments, generally resulting in two NO_x levels, 1.8 ppb NO + 70 ppb NO_2 (Exp.

195 41 – 54) and 4.8 ppb NO + 120 ppb NO_2 (Exp. 55 – 68) at the exit of the OFR. With the aim to

196 slightly modify OH exposure but keep NO_x concentrations constant among each set of

197 experiments, the initial concentrations of 1,3,5-TMB were adjusted in a large range (16.7 – 84.1

198 ppb), as an increase in the precursor concentration corresponds to a larger sink for OH, while

199 RH and irradiances were not changed.

200   A nitrate CIMS (Ehn et al., 2014; Eisele and Tanner, 1993) and a Vocus PTR (Krechmer

201 et al., 2018) were deployed at the exit of the OFR to measure the oxidation products of 1,3,5-

202 TMB. These two mass spectrometers have been well characterized in a previous study (Wang

203 et al., 2020).

204   In this study, the sample flow rate for the nitrate CIMS was 8 slpm through a Teflon tube

205 with an outer diameter (OD) of 1/4 in. and a length of 70 cm. The sheath flow for the nitrate

206 CIMS was supplied by a zero-gas generator at a flow rate of 15 slpm. Mass resolution was

207 approximately 8000 for ions with m/z larger than 200 Th. HOMs generated from TMB

208 oxidation were charged in the ambient pressure interface region by collisions with nitrate

209 clusters, $(HNO_3)_x \cdot NO_3^-$ ($x = 0 – 2$), and detected by nitrate CIMS as clusters with NO_3^-, i.e.,

HOM·NO_3^- (Hyttinen et al., 2015). In addition, HOMs' signals were corrected with relative transmission efficiencies of our nitrate CIMS obtained via a method reported previously (Heinritzi et al., 2016). We followed the same sampling method of PAM OFR as those in previous studies, in order to obtain a similar flow tube residence time distributions (RTDs) and thus validate usage of a modified PAM_chem_v8 model to estimate concentrations of radicals in the OFR as discussed below. We acknowledge that this is not a perfect sampling setting for nitrate CIMS. However, the reduction in the sampling efficiencies of various HOMs is likely to be close, if not identical, which keeps the distributions of HOMs.

Vocus PTR was applied to quantify precursor concentrations and measure volatile and intermediate volatility oxidation products. The focusing ion-molecule reactor (FIMR) was heated up and its temperature was maintained at 100 ℃ during the experiments. The FIMR can be operated under 2.0 mbar without a strong interference from corresponding water clusters when ionizing the neutral compounds. The Vocus front and back voltages were 650 V and 15 V, respectively, forming an axial voltage of 635V and a reduced electrical field (*E/N*, where E is the electric field strength and N is the number density of the buffer gas in FIMR) of 180 Td. The radio frequency (RF) voltages and frequency were set to be 450 V and 1.3 MHz, respectively. The sample flow was introduced to the Vocus PTR through a Teflon tube with an OD of 1/4 in. and a length of 120 cm from the OFR. A total sample flow of 1.4 slpm was maintained by a pump with an orifice to minimize the delay time of sampling, from which approximately 125 sccm was sampled into the FIMR through a capillary tube.

We did not quantify HOMs' concentrations. Since the inner diameters of PAM OFR, sampling tube, and the nitrate CIMS inlet were different, and two reducing unions were used during sampling, the estimation of the penetration efficiency and sampling efficiency of HOMs are of a significant uncertainty. The initial concentrations of TMB utilized in the experiments fluctuated slightly, which resulted from sample preparation processes, but generally were around 50 ppbv. We tried to minimize potential influences of the differences in the initial TMB concentrations on the signals of HOMs by normalizing the HOMs signals with the initial TMB signal. To precisely illustrate changes in the abundance of HOMs at different OH exposures, a normalized signal was chosen to present the abundance of detected HOMs, which is defined as the ratio of the signals of HOMs in the nitrate CIMS normalized by the reagent ions and the initial signal of 1,3,5-TMB, i.e., $S(HOMs)/S(TMB)$. $S(HOMs)$ is the signal of HOM detected by the nitrate CIMS normalized with the signal of reagent ions, whereas $S(TMB)$ is the initial signal of 1,3,5-TMB detected by the Vocus PTR.

To further explore the secondary chemistry in the formation and evolution of HOMs, a nominal relative molar yield of HOMs, defined as $S(HOMs)/k[VOCs][OH]$, was used as a

 ~~substitute of molar HOM yields to reveal their changes under different OH exposures, which is~~
246 ~~similar to the definition from a previous study (Garmash et al., 2020). k, $[VOCs]$, and $[OH]$~~
247 ~~stand for the loss coefficient of HOMs in the OFR timing the calibration factor of the nitrate~~
248 ~~CIMS and then divided by the OH oxidation reaction coefficient of 1,3,5-TMB, 1,3,5-TMB~~
249 ~~concentration detected at the exit of OFR, and calculated OH concentration in the OFR,~~
250 ~~respectively. The detailed derivation processes and calculation methods are provided in~~
251 ~~Supplementary Text S1.~~

To validate our settings, a PAM chemistry model (PAM_chem_v8), utilized widely in previous studies, were chosen with the latest updates to calculate radical profiles in our OFR (Li et al., 2015; Cheng et al., 2021; Wang et al., 2020; Mehra et al., 2020; Lambe et al., 2015, 2018; Peng and Jimenez, 2020; Lambe et al., 2017). This model is based on a photochemical box model that includes chemistry of photolysis of oxygen, water vapor, and other trace gases by the primary wavelengths of mercury lamps, and simplified VOC and RO_2 chemistry (Table S2), but further reactions of the first-generation stabilized products and the second-generation organic radicals are not considered. The detailed reactions involved with RO_2 include:

$$RO_2 + R'O_2 \rightarrow RO + R'O + O_2 \qquad (R1)$$

$$RO_2 + R'O_2 \rightarrow R = O + R'OH + O_2 \qquad (R2)$$

$$RO_2 + R'O_2 \rightarrow ROH + R' = O + O_2 \qquad (R3)$$

$$RO_2 + R'O_2 \rightarrow ROOR' + O_2 \qquad (R4)$$

$$RO_2 + HO_2 \rightarrow ROOH + O_2 \qquad (R5)$$

$$RO_2 + OH \rightarrow Products \qquad (R6)$$

$$RO_2 \xrightarrow{\text{isomerization}} Products \qquad (R7)$$

$$RO_2 + NO \rightarrow RO + NO_2 \qquad (R8)$$

$$RO_2 + NO \rightarrow RONO_2 \qquad (R9)$$
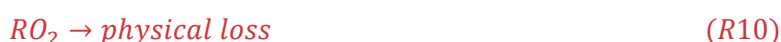
$$RO_2 \rightarrow physical\ loss \qquad (R10)$$

$R1$, $R2$, and $R3$ are reactions of $RO_2 + RO_2$, forming alkoxy radicals, carbonyl termination products, and hydroxyl termination products, respectively. $R4$ is the accretion reaction, forming dimers via combination of two monomeric RO_2. $R5$ is the reaction between RO_2 and HO_2, forming hydroperoxyl radicals. $R6$ is the reaction between OH and RO_2, whose reaction channels/products are proposed according to previous studies (Table S3). $R7$ is the unimolecular reactions of RO_2 in the PAM OFR, among which the autoxidation reaction rate is the most significant. $R8$ and $R9$ are the reactions between NO and RO_2, generating alkoxy radicals and organonitrates, respectively. $R10$ is the physical loss of RO_2.

Kinetic data in the modified PAM_chem_v8 are obtained from the IUPAC (International Union of Pure and Applied Chemistry) dataset (https://iupac-aeris.ipsl.fr, last access: 26

October 2023) and the MCM dataset (MCM v3.3.1, https://mcm.york.ac.uk/MCM/, last access: 9 October 2023), except those that are specifically discussed in details in the supplement. Note that the total RO_2 concentration is simplified to be the sum of concentrations of BPR and $C_9H_{13}O_7\cdot$. In this work, the autoxidation reaction and the accretion reaction of 1,3,5-TMB-derived BPR, as well as the subsequent reactions of the autoxidation product of BPR, i.e., $C_9H_{13}O_7\cdot$, are newly implemented or modified in this model (Reaction No. 41 – 57 in Table S2). The newly implemented or modified reactions in this model are discussed in Supplementary Text S1. NO_x-related reactions are also included in the model. When we simulate experiments without NOx, these reactions do not contribute to the simulation results.

The input parameters of temperature, mean residence time, water vapor concentration, O_3 concentration, and the initial 1,3,5-TMB concentration are 25 °C, 53 s, 0.8%, 500 ppbv, and 50 ppbv, respectively, as measured directly in the experiments. The actinic flux at 254 nm, I_{254}, is constrained by comparing OH exposures by model output and OH exposures estimated by the consumption of 1,3,5-TMB as measured by a Vocus PTR. Consumption of O_3 estimated by the model agrees well with the measured results, with discrepancies being always within 10% at different OH exposures.

3 Results and discussion

3.1 Validation of experiment settings

Concentration profiles of OH, RO_2, and HO_2 as a function of OH exposures in our experiments without NO_x are illustrated in Figure S1a. According to the modified PAM_chem_v8, when OH increased from 1.09×10^8 to 1.57×10^9 molecule cm^{-3}, HO_2 concentrations increased from 7.72×10^8 to 3.18×10^9 molecule cm^{-3}, whereas RO_2 concentrations increased from 4.83×10^9 to 8.48×10^9 molecule cm^{-3}. The radical concentrations in experiments with NO_x (Figure S1b) varied in a similar range, with RO_2 ranging from 3.89×10^9 to 9.34×10^9 molecule cm^{-3}, HO_2 ranging from 3.66×10^9 to 6.82×10^9 molecule cm^{-3}, and OH ranging from 4.83×10^8 to 9.05×10^8 molecule cm^{-3}, respectively. The ratios between HO_2/OH and RO_2/OH in our experiments are displayed in Figure S1c. The HO_2/OH ratio ranged between 1.9 and 7.1 in our PAM OFR experiments without NO_x, and the RO_2/OH ratio ranged between 4.9 and 47.9. In experiments with NO_x, the HO_2/OH ratio ranged between 3.7 and 17.9, whilst the RO_2/OH ratio ranged between 4.0 and 13.2. A recent comprehensive ambient campaign conducted in the wintertime central Beijing reported mean daytime peak concentrations of 8.8×10^7, 3.9×10^7, and 2.7×10^6 molecule cm^{-3} for total RO_2, HO_2, and OH, respectively (Slater et al., 2020), which corresponds to ambient RO_2/OH and HO_2/OH ratios of

314   32.6 and 14.4 (Figure S1c), respectively. Therefore, radical ratios in our flow tube were

315   generally in the same order of magnitude with the ambient conditions.

316
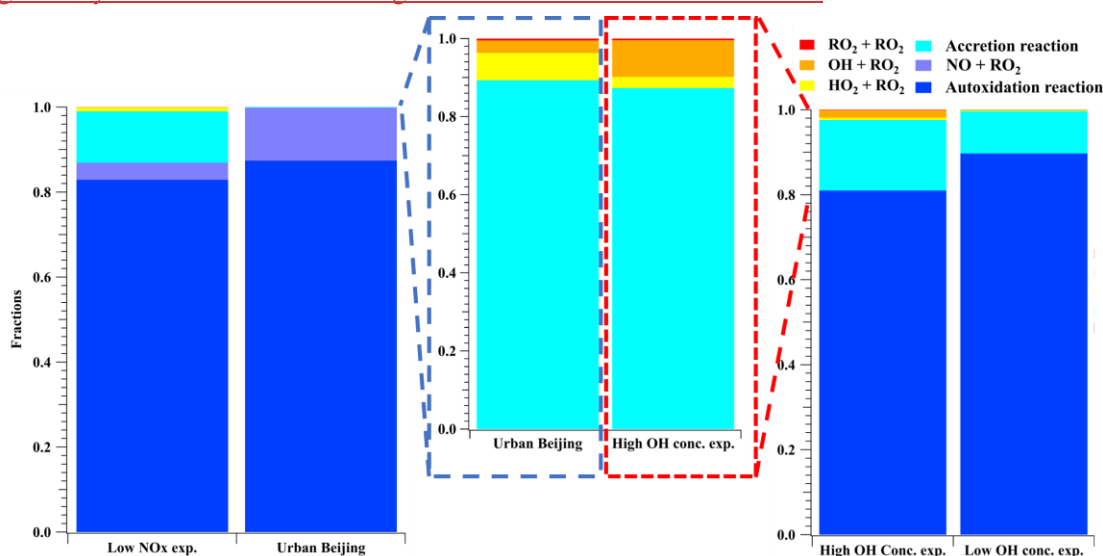
317 **Figure 1.** Fates of RO_2 generated in the low NO_x experiment (Exp. 44), urban Beijing (Slater

318 et al., 2020), low OH and zero NO_x experiment (Exp. 19), and high OH and zero NO_x

319 experiment (Exp. 12). Note that RO_2 fates of RO_2, OH, HO_2, and accretion channels are blown

320 up for a better comparison for urban Beijing and the high OH and zero NO_x experiment.

321 Reactions and kinetic rate coefficients used in the calculations are provided in Table S2.

322

323   We take Exp. 12, 19 and 44 as representative examples and compare simulation results

324 with those from the ambient environment (Slater et al., 2020). The RO_2 lifetime in urban Beijing

325 (Slater et al., 2020), low NO_x experiment, low OH and zero NO_x experiment, and high OH and

326 zero NO_x concentration experiment was 1.0, 0.7, 1.2, and 0.6 s, respectively. As shown in

327 Figure 1, In the low NO_x experiment (Exp. 44), the fractions of $RO_2 + RO_2$ ($R1 – R3$), accretion

328 reaction ($R4$), $RO_2 + HO_2$ ($R5$), $RO_2 + OH$ ($R6$), autoxidation ($R7$), and $RO_2 + NO$ ($R8 – R9$)

329 were 0.06%, 12.1%, 0.9%, 0.07%, 82.9%, and 4.0%, respectively. Calculated based on the

330 mean daytime peak concentrations of radicals in Beijing (Slater et al., 2020), the fractions of

331 $R1 – R3$, $R4$, $R5$, $R6$, $R7$, and $R8 – R9$ were 0.0005%, 0.09%, 0.007%, 0.003%, 87.4%, and

332 12.5%, respectively. For the experiment with low OH and zero NO_x (Exp. 19), the fractions of

333 $R1 – R3$, $R4$, $R5$, $R6$, and $R7$ were 0.05%, 10.0%, 0.15%, 0.14%, and 89.7%, respectively. For

334 the one with high OH and zero NO_x (Exp. 12), the fractions of $R1 – R3$, $R4$, $R5$, $R6$, and $R7$

335 were 0.08%, 16.6%, 0.54%, 1.8%, and 81.0%, respectively. The overall lifetimes of RO_2 and

336 the fractions of autooxidation together determine the significant and similar roles of

337 autoxidation in both laboratory experiments and the ambient. Therefore, the autoxidation chain

338 will run to a similar oxidation level between the laboratory and the ambient.

339   In experiments with NO_x (e.g., Exp. 44), though the yields of organonitrates were lower in

340   the laboratory experiments, the formation pathways of these compounds were the same as those

341   in the ambient. Based on the formulae of organonitrates, the detailed formulae for monomer

342   RO_2 could be probed, which helps to investigate the existence of multi-generation OH oxidation.

343   Alkoxy radicals generated in the NO termination channel will unlikely influence the

344   distributions of C9 stabilized products since they tend to get decomposed in the subsequent

345   reactions, as discussed in the Supplementary Text S1.

346   In experiments in absence of NO_x (e.g., Exp. 12 and 19), the proportions of $R8$ - $R9$, i.e.,

347   the NO channel in urban environment were reassigned to termination reactions of $R1$ - $R6$, i.e.,

348   RO_2 + RO_2, accretion reaction, RO_2 + HO_2, and RO_2 + OH. Comparison of relative fractions of

349   RO_2 fates of RO_2, OH, HO_2, and accretion channels (Figure 1) shows similarities between

350   laboratory and ambient results. By expanding proportions of these termination reactions,

351   laboratory investigations on distributions of products can be facilitated, as the detection of

352   certain HOM products became more precise and the mass spectra became simplified. As

353   discussed in the "results" session, products of $R2$, $R3$, and $R5$ channels of the main BPR were

354   not detected in our experiments due to their low oxygen contents, while secondary products

355   between products of $R2$, $R3$, and $R5$ channels of the main BPR and OH were observed.

356   Together with stabilized products and secondary products from $C_9H_{13}O_7\cdot$ (the peroxy radical

357   formed from autooxidation of BPR), secondary products between products of $R2$, $R3$, and $R5$

358   channels of the main BPR and OH help to elucidate the first- and multi-generation reaction

359   pathways in the 1,3,5-TMB+OH system, according to their molecular formular.

360   On the other hand, the much-expanded proportion of HOM dimers through accretion

361   reactions makes it inadequate to compare yields of HOM dimers and HOM monomers.

362   However, identification of HOM dimers can help us identify the exact RO_2 in the OFR and

363   confirm the conditions of secondary OH oxidation according to the number of hydrogen atoms

364   in the molecules.

365   3.2 Oxidation products

366   A total of 33 HOM monomers with formulae of $C_{7-9}H_{8-16}O_{6-11}$ and 22 HOM dimers with

367   formulae of $C_{17-18}H_{24-30}O_{8-14}$ were observed in the gas phase OH-initiated oxidation of 1,3,5-

368   TMB in the OFR, as listed in Table ~~S2~~S4. The relative signal contributions of HOMs to the

369   total signals of all HOMs at an OH exposure of 2.38×10^{10} molecules cm^{-3} s are listed as an

370   example in Table ~~S2~~S4. The most abundant HOM products were also shown in stack in Figure

371   2. ~~Figure 1 illustrates how OH exposures in the OFR are related to the total normalized signals~~

372   ~~of HOM monomers and HOM dimers measured at the OFR exit, which is~~ whose relationships

373   with OH exposures are superimposed by a gamma function ($f(x) = ax^m e^{-x}$) simulation line

374   to guide the eyes. The sum of normalized HOM monomers' abundance increased

375   monotonically up to the highest OH exposure of 5×10^{10} molecule cm^{-3} s, whereas those of

376   HOM dimers showed a non-monotonic dependence on OH exposure. The observed faster

377   increase of accretion products than that of HOM monomers can be explained jointly by the fast

378   second-order kinetics for accretion reactions of RO_2 (Berndt et al., 2018b) and the high

379   concentrations of relevant radicals in this work. On the other hand, most of the first-generation

380   HOM dimers formed from accretion reactions contain at least one C=C bond and have more

381   functionalities than HOM monomers, and thus should be more reactive to OH radicals, which,

382   together with a faster deposition loss of dimers, results in a faster consumption of HOM dimers

383   than monomers in the OFR. The faster production and consumption of HOM dimers allowed

384   their concentrations to summit at middle levels of OH exposures. Because of the inherent

385   disadvantage of laboratory experiments, RO_2 concentrations are always too high in the OFR,

386   which has been pointed out in a previous study (Bianchi et al., 2019). The accretion reactions

387   in the OFR are relatively more significant than it should be in the ambient atmosphere. We do

388   not mean to compare HOM monomer and HOM dimer signals crossly here, but to pay attention

389   to their formulae.

390   (a)
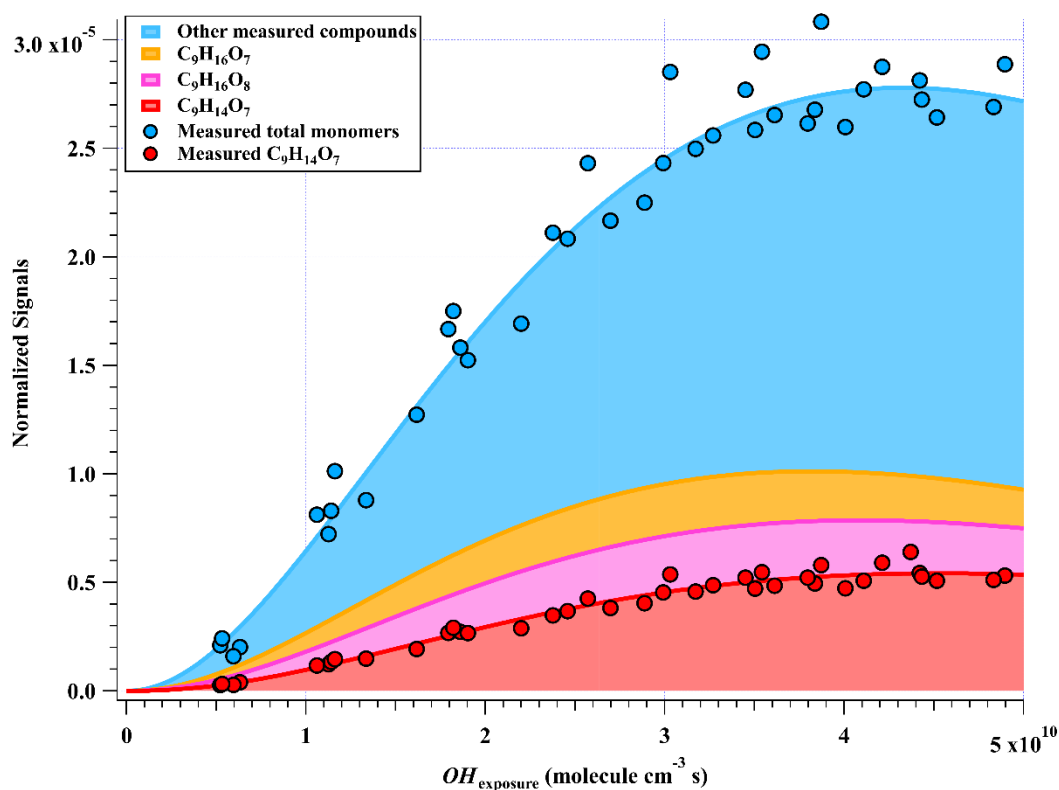
391

392   (b)
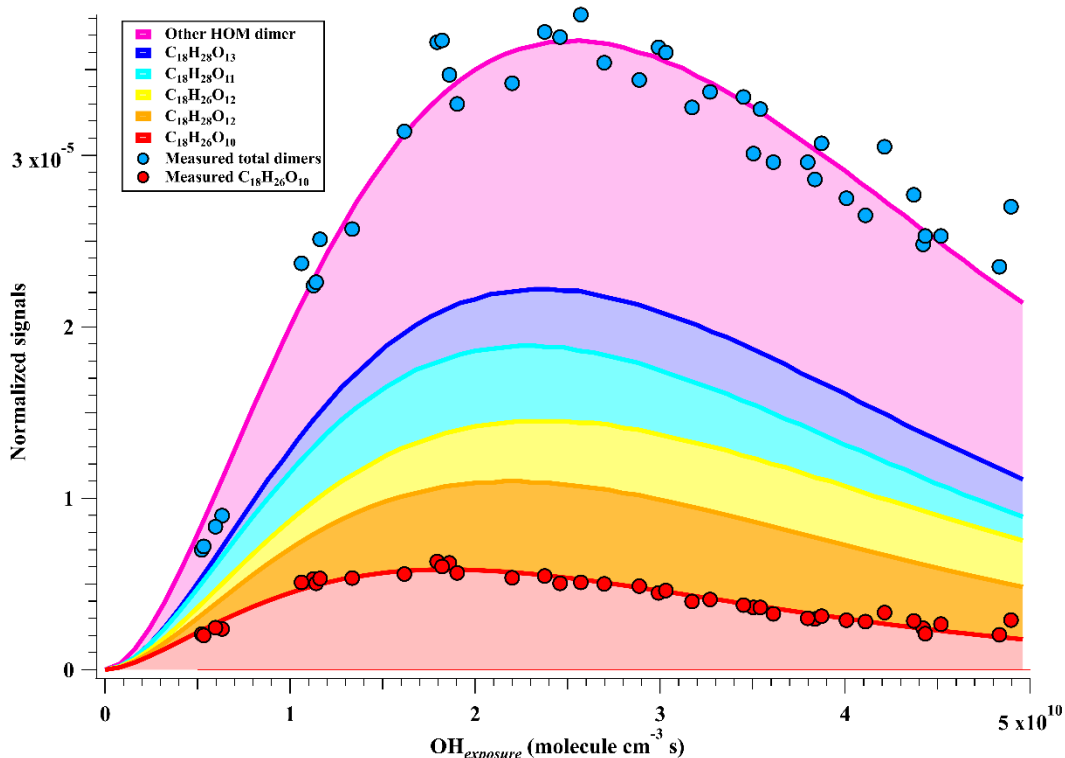
Figure 2. Normalized signals of (a) HOM monomers and (b) HOM dimers versus OH exposure that are fitted via a gamma function and shown in stacked.

Theoretically, at a given RH and UV (i.e., a given OH), an increase in the initial TMB would lead to formation of more RO_2, which corresponds to a larger RO_2/OH. However, under our experimental conditions, the $RO_2/OH/HO_2$ channels of RO_2 radicals are always minor, and thus an increase in RO_2/OH would not have a significant impact on the relative distribution of products formed from these channels We compared product MS for experiments with a similar OH exposure but different initial concentrations of TMB (e.g., Exp. 3 v.s. Exp. 19, and Exp. 12 v.s. Exp. 22). The OH exposures of Exp. 3 and Exp. 19 were estimated by the modified PAM_chem_v8 model to be 5.2×10^9 and 5.3×10^9 molecule cm^{-3} s, respectively, but the initial concentration of TMB of Exp. 3 was 25% more than that in Exp. 19. Meanwhile, the OH exposures of Exp. 12 and Exp. 22 were 4.5×10^{10} and 4.4×10^{10} molecule cm^{-3} s, respectively, but the initial concentration of TMB of Exp. 12 was 48% more than that in Exp. 22. Comparisons between the product MS of Exp. 3 and Exp. 19 (Figure S2), as well as of Exp. 12 and Exp. 22, show that increase in the initial concentration of precursors generally resulted in a minor increment in the absolute signals of HOMs. Clearly, the relative distributions of products in these experiments are quite similar, indicating a minor difference in the relative distributions of products caused by fluctuations of initial concentrations of TMB.

3.2.1 HOM monomers ~~in the absence of NO~~$_x$

414   Previous studies indicate that oxidation products derived from the peroxide-bicyclic

415   pathway represent a main fraction of HOMs (Wang et al., 2017; Zaytsev et al., 2019). For 1,3,5-

416   TMB, this pathway, as recommended by Master Chemical Mechanism (MCM), starts from a

417   BPR, $C_9H_{13}O_5\cdot$ (MCM name: TM135BPRO2) (Molteni et al., 2018). Scheme 1 has been

418   proposed to provide a good understanding of this reaction system and the structures of oxidation

419   products. Molteni et al. (2018) suggested that $C_9H_{13}O_7\cdot$, i.e., peroxy radical formed from

420   autooxidation of $C_9H_{13}O_5\cdot$ has two isomers~~, which are referred as C9H13O7A and C9H13O7B~~

421   ~~for clarity in this study. The structures of these two isomers have been provided in Scheme 1.~~

422   ~~Their termination products are nominated according to the name of these two isomers,~~

423   ~~respectively~~. A second-step of endo-cyclization is required in the formation of one of the isomer,

424   which is extremely slow and not competitive as shown in several previous studies using both

425   experimental and theoretical approaches (Wang et al., 2017; Xu et al., 2020). Even if such a

426   second O_2 bridging to a double bond is assumed to be possible, the abundance of this isomer

427   should be significantly smaller than the other one, because of the much faster reaction rate of

428   H-shift reaction. Therefore, we do not take the $C_9H_{13}O_7\cdot$ isomer containing a double endo-

429   cyclization into consideration in this work. The majority of HOM monomers is generated from

430   subsequent reactions of $C_9H_{13}O_5\cdot$ and newly formed $C_9H_{13}O_7\cdot$. ~~A second step of endo-~~

431   ~~cyclization is required in the formation of C9H13O7B, which is extremely slow and not~~

432   ~~competitive as shown in several previous studies using both experimental and theoretical~~

433   ~~approaches (Wang et al., 2017; Xu et al., 2020). Even if such a second O₂ bridging to a double~~

434   ~~bond is assumed to be possible, the abundance of C9H13O7B should be significantly smaller~~

435   ~~than C9H13O7A, because of the much faster reaction rate of H-shift reaction in the reaction~~

436   ~~route for C9H13O7A. Therefore, the majority of HOM monomers are generated from~~

437   ~~subsequent reactions of C₉H₁₃O₅· and C9H13O7A,~~ both of which contain one C=C bond in the

438   carbon backbone and thus have a feasible site for OH addition. Meanwhile, the autoxidation

439   reaction rate for newly formed $C_9H_{13}O_7\cdot$~~C9H13O7A~~ should be significantly smaller than

440      $C_9H_{13}O_5\cdot$, as there is no hydrogen atom in $C_9H_{13}O_7\cdot$ that is able to undergo a hydrogen atom

441   shift at an appreciable rate based on our current understanding. Therefore, the subsequent

442   autoxidation reaction should not be able to generate large amounts of more oxidized RO_2.
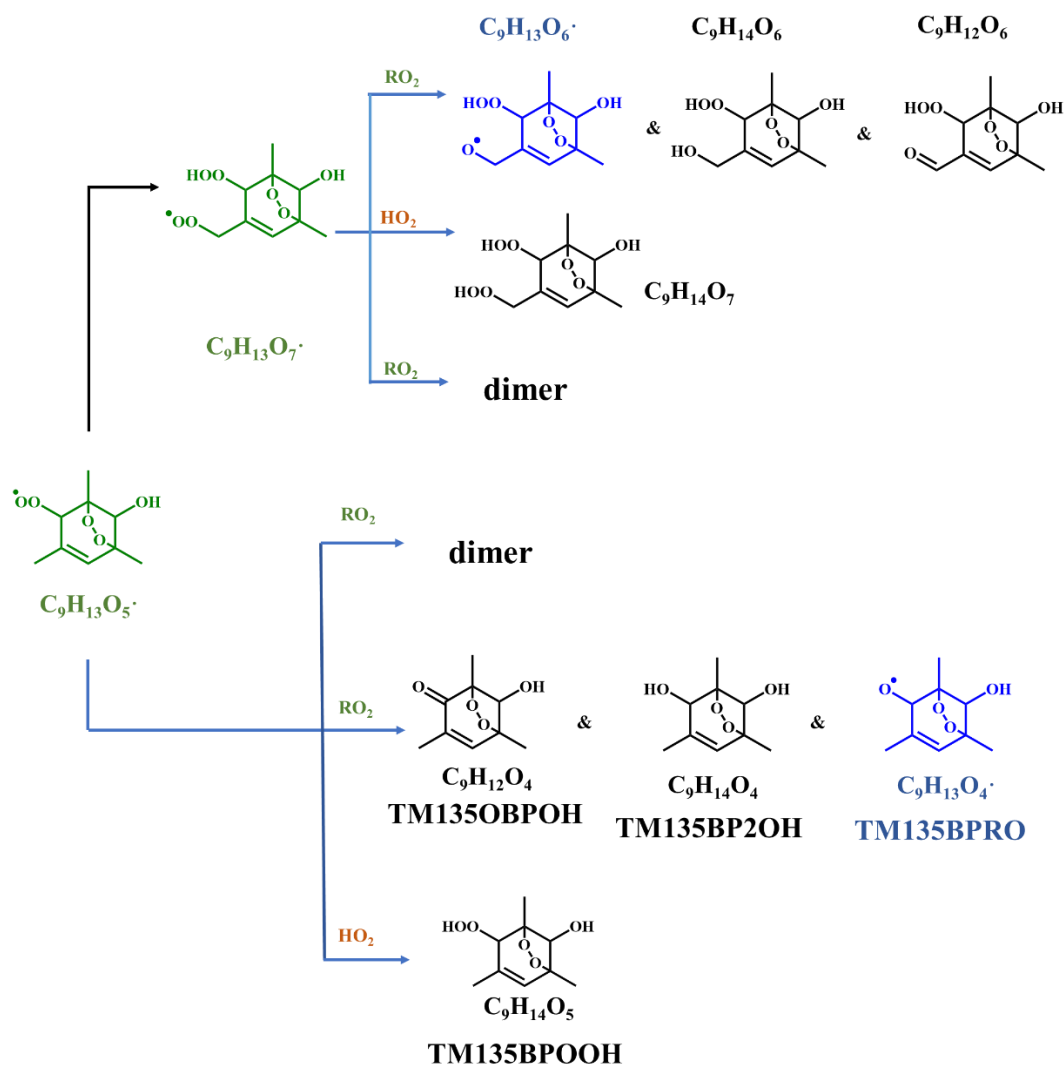
Scheme 1. Oxidation pathways of the bicyclic peroxy radical $C_9H_{13}O_5\cdot$ (MCM name: TM135BPRO2) in the OH-initiated oxidation of 1,3,5-TMB. Green, blue, and black formulae denote alkyl peroxy radicals, alkoxy radicals and stabilized products, respectively. Black arrows denote the autoxidation pathway. MCM names for HO_2- and RO_2-termination products of TM135BPRO2 are present.

The monomeric termination products of BPR, as shown in Scheme 1, were not detected by nitrate CIMS due to their own low oxygen content and thus relative low detection efficiency in nitrate CIMS, which has been investigated in a previous study (Riva et al., 2019).were not detected by nitrate CIMS because of their low oxygen content, whereas t Those of $C_9H_{13}O_7\cdot$ were all observed clearly, including $C_9H_{12}O_6$, $C_9H_{14}O_6$, and $C_9H_{14}O_7$. Especially, $C_9H_{14}O_7$ was the most abundant one among all of the HOM monomer products (Figure 2a). As proved by a previous study, these three species should be typical first-generation stabilized products derived from autoxidation (Wang et al., 2020). Their nominal relative molar yields

458 ~~increased with the OH exposures in the OFR, as shown in Figure S1, which implies that the~~

459 ~~secondary OH reactions of stabilized products can also produce these HOM monomers~~

460 ~~otherwise the observed yields would remain constant or decline (, the latter of which is due to~~

461 ~~the consumption of the products).~~ These HOM monomers ~~thus~~ should consist of several isomers

462 bearing the same formula, because products from the secondary reactions cannot share the same

463 structure as that of the one from the first-generation reaction. However, limited by the inherent

464 disadvantages of mass spectrometers, we could not distinguish isomers here and further

465 illustrate their different chemical behaviors.

466 In addition to these three ones, the ~~nominal relative molar yields of other HOM monomers~~

467 ~~also showed an increase trend with more OH exposures. The~~ next most prominent products to

468 $C_9H_{14}O_7$ were $C_9H_{16}O_7$ and $C_9H_{16}O_8$ (Figure ~~2a~~3a), which are produced from multi-generation

469 oxidation according to their hydrogen content (Molteni et al., 2018; Cheng et al., 2021). Based

470 on the formulae of these three HOM monomers, they ($C_9H_{14}O_7$, $C_9H_{16}O_7$, and $C_9H_{16}O_8$) could

471 be formed from the bimolecular termination reactions of $C_9H_{15}O_8\cdot$, which can be generated by

472 an OH attack to $C_9H_{14}O_5$ (Scheme 2), the hydroperoxyl termination product of the BPR

473 $C_9H_{13}O_5\cdot$. The other HOM monomers characterized with high signals were $C_9H_{14}O_8$ and

474 $C_9H_{16}O_9$ (Figure ~~2b~~3b). These two HOM monomers ($C_9H_{14}O_8$ and $C_9H_{16}O_9$), together with

475 $C_9H_{16}O_8$, correspond to the monomeric termination products of $C_9H_{15}O_9\cdot$, which is highly likely

476 the peroxy radical generated by an OH attack to $C_9H_{14}O_6$ (Scheme 3), i.e., the hydroxyl

477 termination product of $C_9H_{13}O_7\cdot$. As discussed earlier, $C_9H_{13}O_7\cdot$ is a typical autoxidation

478 reaction product of the BPR of $C_9H_{13}O_5\cdot$. Therefore, detected signals of $C_9H_{16}O_8$ should be the

479 sum of two isomers' signals at least. Other HOM monomers were generally observed at much

480 lower signals and thus were not plotted individually.

481 (a)

482

483 (b)

484
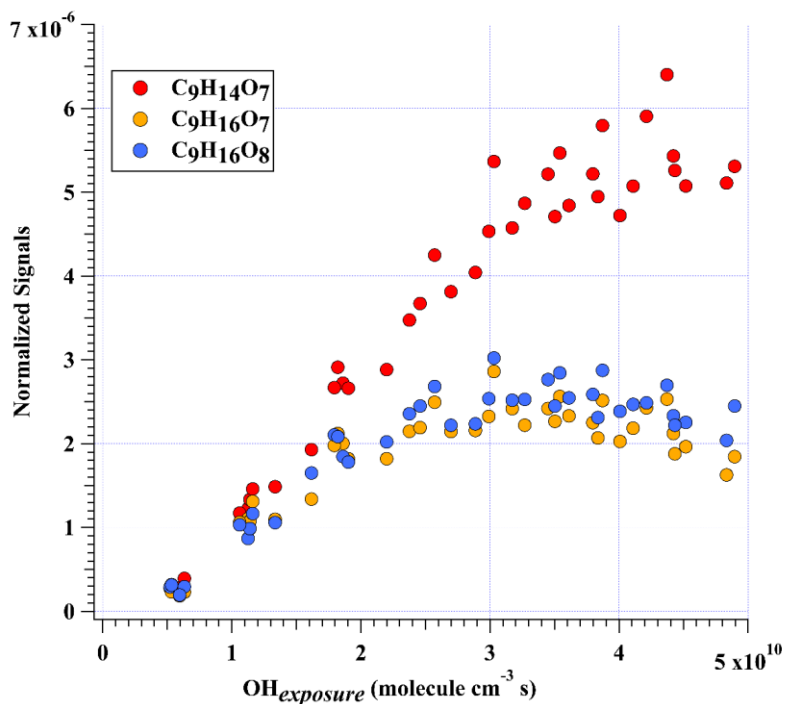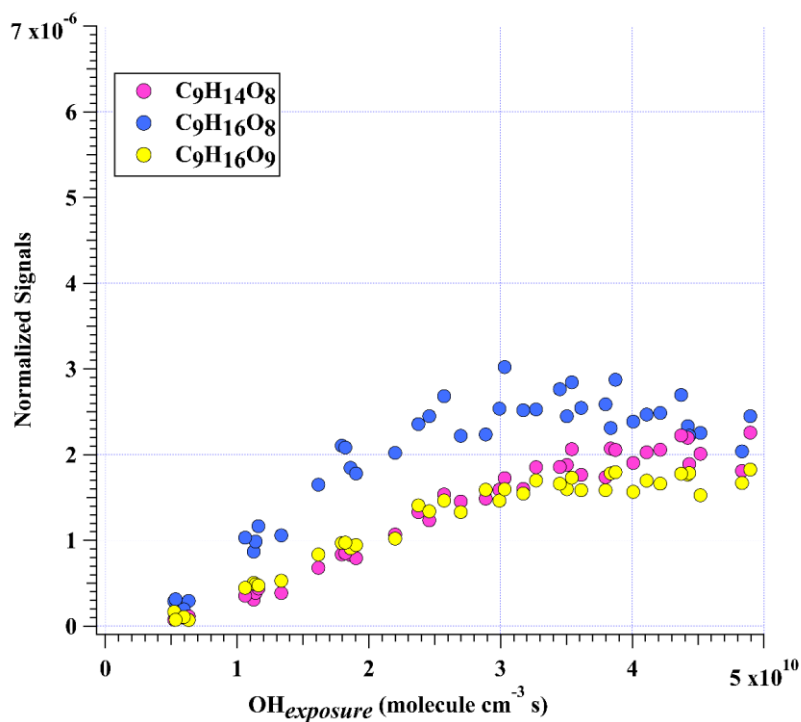
Figure 3. Normalized signals of (a) $C_9H_{14}O_7$, $C_9H_{16}O_7$, and $C_9H_{16}O_8$ and (b) $C_9H_{14}O_8$, $C_9H_{16}O_8$, and $C_9H_{16}O_9$ measured at the exit of OFR in experiments without NO_x as a function of OH exposure. $C_9H_{16}O_8$ are shown in both plots to better illustrate the chemical profiles of different compound groups.

489
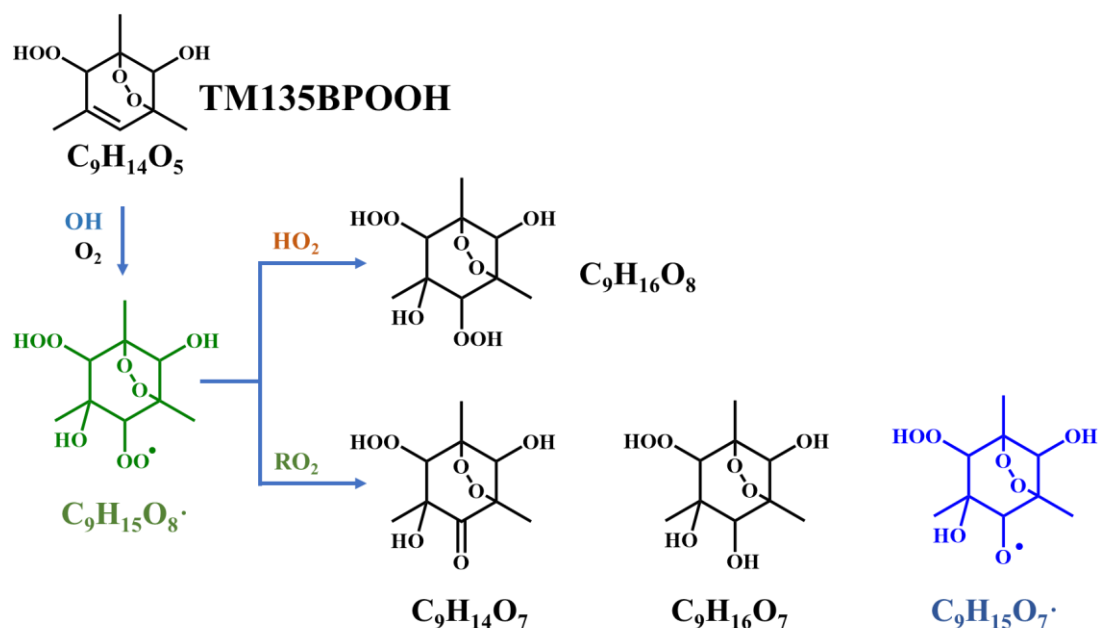
Scheme 2. Proposed formation pathways of $C_9H_{14}O_7$, $C_9H_{16}O_7$, and $C_9H_{16}O_8$ via the secondary
OH oxidation of TM135BPOOH.

492
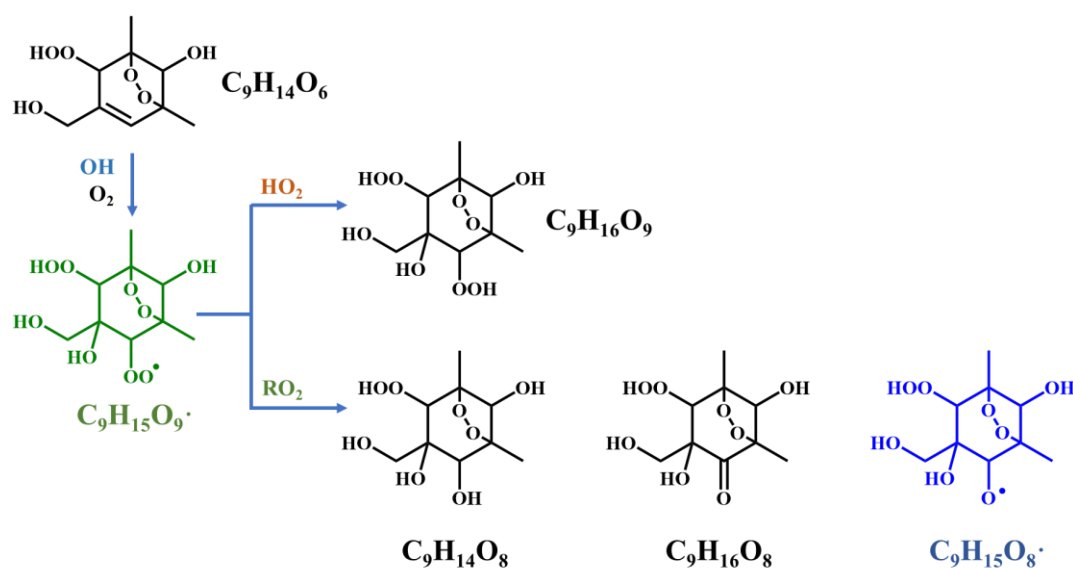
Scheme 3. Proposed formation pathways of $C_9H_{14}O_8$, $C_9H_{16}O_8$, and $C_9H_{16}O_9$ via the secondary
OH oxidation of TM135BPOOH.

We further examined the nominal relative molar yields of HOM products with 12, 14, and
16 hydrogen atoms, i.e., the common HOM monomers in our system. Based on the number of
hydrogen atoms, $C_9H_{12}O_m$ (m refers to the oxygen atom number in a molecule) are presumably
derived from first-generation radicals of $C_9H_{13}O_m\cdot$, and $C_9H_{16}O_m$ are from second-generation
radicals of $C_9H_{15}O_m\cdot$, whereas $C_9H_{14}O_m$ can be either products of the first-generation or second-
generation OH oxidation (Molteni et al., 2018). Therefore, compounds with more hydrogen
atoms are expected to increase more rapidly. However, the actual observation in our laboratory

502 ~~experiments conflicted with our preconceived expectations. The nominal relative molar yields~~
503 ~~of HOM monomers are shown in Figure 3. For clarity, only the 3 most abundant species with~~
504 ~~(a) 12, (b) 14, and (c) 16 hydrogen atoms, respectively are plotted. A prominent linear increase~~
505 ~~in the nominal molar yields of $C_9H_{14}O_m$ with larger oxygen atom numbers and $C_9H_{16}O_m$ was~~
506 ~~observed with the increase of OH exposure, whereas $C_9H_{14}O_m$ with fewer oxygen atoms and~~
507 ~~$C_9H_{12}O_m$ increased convexly. This is likely because the concentrations of RO_2 in the OFR~~
508 ~~increased with the increment of consumed precursors, which promoted the carbonyl and~~
509 ~~hydroxyl channels and favored formation of $C_9H_{12}O_m$ and $C_9H_{14}O_m$ with fewer oxygen atoms~~
510 ~~in the molecule.~~

511 It is worth noting that HOM monomers with 18 hydrogen atoms were never observed in
512 our experiments, including a potential stabilized hydroperoxyl products formed from $C_9H_{17}O_m\cdot$.
513 This is expected, since $C_9H_{17}O_m\cdot$ should be in really low concentrations, if ever existed. As
514 indicated by its hydrogen number, a $C_9H_{17}O_m\cdot$ was formed by at least two OH additions to the
515 C=C bond of a $C_9H_{13}O_m\cdot$, but the main BPR, $C_9H_{13}O_5\cdot$, and its autoxidation product ($C_9H_{13}O_7\cdot$),
516 are characterized with one C=C bond on the ring, which makes this formation pathway
517 impossible. Other ring-breakage pathways should not contribute to the formation of this radical
518 ($C_9H_{17}O_m\cdot$) because of their low branching ratio as determined by recent studies (Zaytsev et al.,
519 2019; Xu et al., 2020).

520 Scheme 4 shows the NO termination pathways of the main BPR $C_9H_{13}O_5\cdot$ and its
521 autoxidation product, $C_9H_{13}O_7\cdot$. After introducing N_2O into PAM OFR, quantities of
522 organonitrates were generated, including both C9 and C18 organonitrates. The averaged mass
523 spectrometry of nitrate CIMS in the 1.8 ppb NO experiment and 4.8 ppb NO experiment is
524 shown in Figure S3. Organonitrates were formed via the NO + RO_2 reaction, called as NO
525 termination reactions. The distribution of oxidation products under these two NO settings were
526 similar.
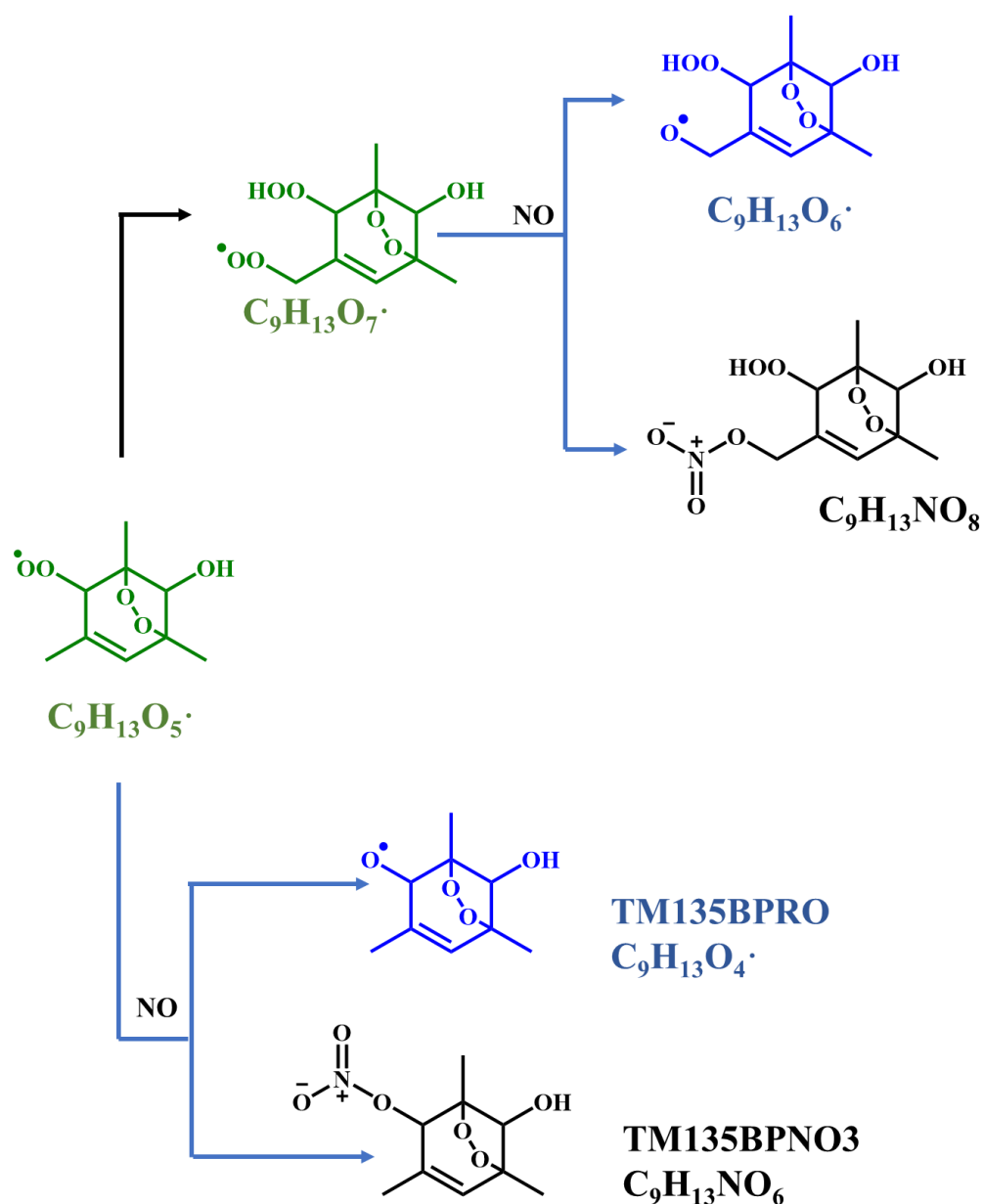
Scheme 4. NO termination reactions of the bicyclic peroxy radical $C_9H_{13}O_5\cdot$ (MCM name: TM135BPRO2) and its autoxidation reaction products. Green, blue, and black formulae denote alkyl peroxy radicals, alkoxy radicals and stabilized products, respectively. Black arrows denote the autoxidation pathway. MCM names of NO-termination products of TM135BPRO2 are present.

As discussed above, most of the first-generation HOMs should contain a C=C bond in the carbon backbone. The ubiquitous existence of organonitrates that contain two nitrogen atoms exactly confirms the extensive secondary OH oxidation in the systems, because the NO termination reaction of RO_2 is the only pathway that can generate organonitrates in our experiments and this pathway can only introduce one nitrogen atom at a time, as indicated in

Scheme 4. RO_2 can react with NO_2 to form peroxynitrates ($ROONO_2$) but these species are thermally unstable except at very low temperatures or when the RO_2 is an acylperoxy radical (Orlando and Tyndall, 2012), neither of which were not met in our experiments. The concentrations of NO_3 were estimated to be lower than 1 pptv by our modified PAM_chem_v8 because of the existence of decent concentrations of NO, which would consume NO_3 at a rapid reaction rate, i.e., 2.7×10^{-11} molecule^{-1} cm^3 s^{-1} (IUPAC dataset , https://iupac-aeris.ipsl.fr, last access: 26 October 2023). Therefore, NO_2 and NO_3 were not likely to react with RO_2 to form large amounts of organonitrates in our experiments. Taking the most abundant organonitrate, $C_9H_{14}N_2O_{10}$, as an example, it was exactly the NO termination product of $C_9H_{14}NO_9\cdot$, which was generated from an OH attack and a subsequent O_2 addition to $C_9H_{13}NO_6$, the NO termination product of $C_9H_{13}O_5\cdot$. For other organonitrates, $C_9H_{13}NO_8$, the second most abundant organonitrate, could be either a NO termination product of $C_9H_{13}O_7\cdot$ or, together with other most abundant organonitrates, $C_9H_{15}NO_7$ and $C_9H_{15}NO_8$, classical termination products of $C_9H_{14}NO_9\cdot$.

The NO:RO_2 ratio in the PAM OFR is lower than typical values in the ambient atmosphere, which is due to the existence of O_3 that was utilized to generate $O(^1D)$ in the OFR and its rapid reaction rate with NO. However, due to rapid reaction rate constants between NO and RO_2, i.e., around 8.5×10^{-12} molecule^{-1} cm^3 s^{-1}, the reaction rate for the NO termination channel of RO_2 was as fast as around $0.3 – 1.0$ s^{-1}. Large amounts of organonitrates would still be formed. Our conclusion is also valid because of detection of compounds with multiple nitrogen atoms.

3.2.2 HOM dimers in the absence of NO.

Accretion reaction $RO_2 + RO'_2 \rightarrow ROOR' + O_2$ is a source of gas-phase dimer compounds from highly oxidized, functional RO_2 radicals.(Ehn et al., 2014; Berndt et al., 2018b; Zhao et al., 2018; Berndt et al., 2018a) $C_{18}H_{26}O_8$ and $C_{18}H_{26}O_{10}$ are two typical accretion reaction products in the 1,3,5-TMB + OH system, whose formation pathways have been elucidated.(Berndt et al., 2018b) $C_{18}H_{26}O_8$ can only be formed via the accretion reaction of two $C_9H_{13}O_5\cdot$. $C_9H_{13}O_3\cdot$ is not likely to react with $C_9H_{13}O_7\cdot$ to form large amounts of $C_{18}H_{26}O_8$. $C_9H_{13}O_3\cdot$ can only be formed after addition of a hydroxyl radical to the aromatic ring of 1,3,5-TMB and a subsequent O_2 addition to the newly formed hydroxyl-substituted cyclohexadienyl radical (Vereecken, 2019). However, the lifetime of this radical is extremely short, as $C_9H_{13}O_3\cdot$ will undertake a ring-closure reaction and get attached by a O_2 very rapidly, forming BPR, $C_9H_{13}O_5\cdot$. Its short lifetime and low concentration, as indicated by Berndt et al. (2018), lead to its insignificant role in the accretion reactions. In contrast, $C_{18}H_{26}O_{10}$ can be formed either by the accretion reaction between $C_9H_{13}O_5\cdot$ and $C_9H_{13}O_7\cdot$ or via a second OH attack to $C_{18}H_{26}O_8$. These two HOM dimers are so far the only ones that are confirmed to be formed via the

574 accretion reactions (Berndt et al., 2018b; Bianchi et al., 2019). There are currently no evidences

575 supporting that $C_9H_{15}O_m\cdot$ radicals can participate in the formation of HOM dimers with 28

576 hydrogens. Therefore, it hints that one could attribute the formation of $C_{18}H_{28}O_m$ to multi-

577 generation OH oxidation of $C_{18}H_{26}O_m$.

578      $C_{18}H_{26}O_{10}$ was characterized with the highest dimer signals for experiments with OH

579 exposures under 3.5×10^{10} molecule cm^{-3} s. Nevertheless, $C_{18}H_{26}O_{10}$, together with $C_{18}H_{28}O_{12}$,

580 $C_{18}H_{26}O_{12}$, $C_{18}H_{28}O_{11}$, $C_{18}H_{28}O_{13}$, and $C_{18}H_{28}O_{10}$ contributed more than 50% of total HOM

581 dimer signals at any OH exposure levels (Figure S22b). These six most abundant HOM dimers

582 correspond exactly to the hydroperoxyl, hydroxyl, and carbonyl termination products of

583 $C_{18}H_{27}O_{11}\cdot$ and $C_{18}H_{27}O_{13}\cdot$, respectively. These two RO_2 ($C_{18}H_{27}O_{11}\cdot$ and $C_{18}H_{27}O_{13}\cdot$), on the

584 other hand, could be generated by OH attacks to $C_{18}H_{26}O_8$ and $C_{18}H_{26}O_{10}$, respectively, which

585 strongly suggests the significant role of secondary OH chemistry in the formation of HOMs in

586 our experiments. In addition, $C_{18}H_{28}O_x$ can also be formed through accretion of a $C_9H_{13}O_m\cdot$

587 radical and a $C_9H_{15}O_m\cdot$ radical, as suggested by previous studies (Molteni et al., 2018; Wang et

588 al., 2020; Tsiligiannis et al., 2019). However, since a $C_9H_{15}O_m\cdot$ radical, as suggested by its

589 hydrogen atom number, can only be formed via an OH addition to the stabilized $C_9H_{14}O_m$

590 products through multi-generation OH reactions, our conclusion that $C_{18}H_{28}O_x$ are multi-

591 generation OH oxidation products still holds. Figure 4 shows the normalized signals of these

592 abundant HOM dimers at different OH exposures. These HOM dimers increased under low OH

593 exposure levels but decreased with the increasing OH exposure that corresponds to 2.8 – 6.9

594 hours' atmospheric equivalent photochemical age.

595 (a)
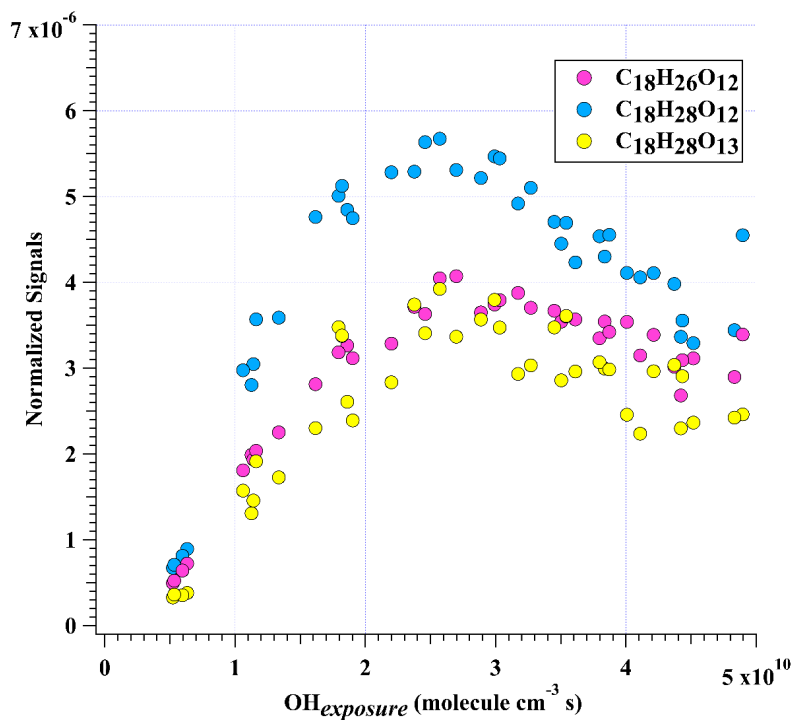
596

597 (b)
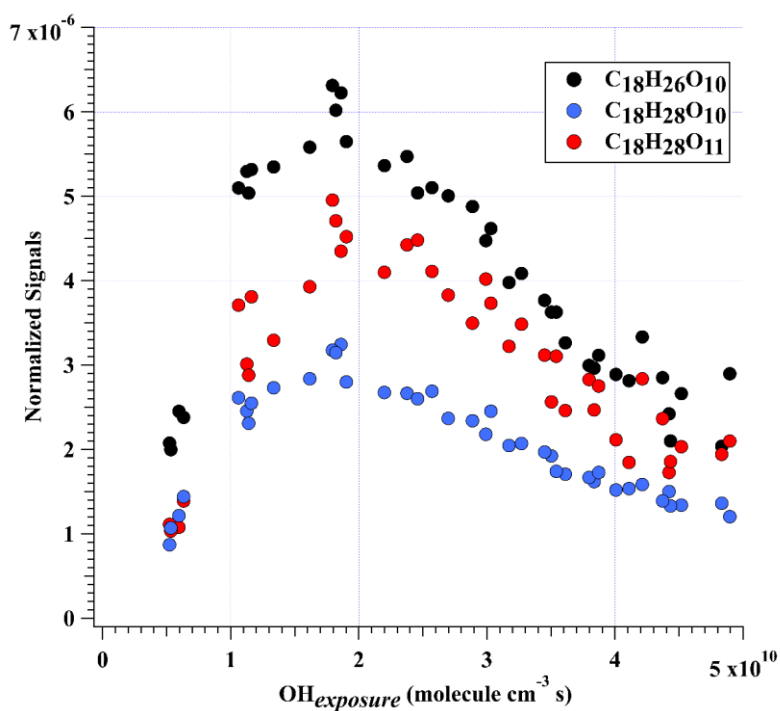
598

Figure 4. Normalized signals of (a) $C_{18}H_{26}O_{12}$, $C_{18}H_{28}O_{12}$, and $C_{18}H_{28}O_{13}$, and (b) $C_{18}H_{26}O_{10}$, $C_{18}H_{28}O_{10}$, and $C_{18}H_{28}O_{11}$ measured at the exit of OFR in experiments without NO_x as a function of OH exposure.

603   This decrease of dimer at relatively high OH exposures are likely due to the accelerated

604 accretion reactions in the OFR, resulted by the high RO_2 concentrations. The HOM dimers are

formed earlier compared to under ambient conditions and then can go through the further oxidation reactions. Note that this does not mean the maximum concentrations of HOM dimers will also accurately occur at the same OH exposures in the atmosphere, because the detailed appearance time of the maximum concentrations of HOM dimers is dependent on their formation rate and loss rate. In our experiments, the formation rate and loss rate were not accelerated equally. On the other hand, the loss pathways of HOM dimers were not exactly the same as the ambient due to the lack of aerosols in the OFR. With the decrease of particulate pollution and thus condensation sinks in the polluted areas, the physical loss of HOMs might be lower and the chemical process can be more important. This series of experiments are not meant to specifically find out the detailed OH exposures when the maximum concentrations of HOM dimers will occur, but try to indicate how HOM dimers evolve with the increase of OH exposures. This work can be regarded as an indicator for the potential chemical fates of HOM dimers in the atmosphere.

The nominal relative molar yields of the abovementioned HOM dimers are shown in Figure 5 as a function of OH exposure, except for $C_{18}H_{28}O_{11}$. The nominal relative molar yields of $C_{18}H_{28}O_{11}$ are not plotted in the Figure 5, since they overlapped quite closely with those of $C_{18}H_{26}O_{10}$, as can be deduced from Figure 4b. Compared with HOM monomers, variation tendencies of the nominal relative molar yields of HOM dimers are more diverse. Especially, the nominal relative molar yield of $C_{18}H_{26}O_8$ (Fig. S3) kept declination under growing OH exposure conditions, whereas that of $C_{18}H_{26}O_{10}$ (Fig. 5) appeared to reduce after a slight growth in the OH exposure range studied. The changes in the nominal relative molar yields of these two HOM dimers along with the OH exposure confirm the combined influences of accretion reactions and multi-generation OH oxidation reactions on their formation and evolution, i.e., further OH oxidation consumed $C_{18}H_{26}O_8$ and $C_{18}H_{26}O_{10}$, and produced $C_{18}H_{26}O_{10}$, $C_{18}H_{26}O_{12}$, $C_{18}H_{28}O_{10}$, $C_{18}H_{28}O_{11}$, $C_{18}H_{28}O_{12}$ and $C_{18}H_{28}O_{13}$. These six HOM dimers contributed the majority of the total HOM dimer signals as mentioned above, while most of them were HOM dimers with 28 hydrogen atoms.

The nominal relative molar yields of dimer compounds with 28 hydrogen atoms tended to increase with extended OH exposures, except that $C_{18}H_{28}O_{10}$ appeared to keep constant when OH exposure was larger than 1×10^{10} molecules cm^{-3} s. This again indicates that these H28 products might be formed by an OH addition to a C=C bond in the accretion products, and then the newly formed alkyl radical further reacted and would go through the typical RO$_2$ termination reactions.

It should be noted that the gas-phase chemistry in the PAM OFR cannot be exactly the same as that in the ambient. Reactions of OH with OVOCs often lead to HO$_2$ formation,

resulting in a $HO_2:RO_2$ ratio larger than 1 in the real atmosphere (Bianchi et al., 2019). A recent campaign conducted at a rural site in the Yangtze River Delta estimated that the local ratio of $HO_2:RO_2$, the latter of which was presumably derived from longer chain alkanes ($> C_3$), alkenes, and aromatic compounds, was around 1.66 (Ma et al., 2022). Such a high $HO_2:RO_2$ ~~$OH:HO_2$~~ ratio condition is typically difficult to be simulated in the laboratory experiments, as the precursors are usually hydrocarbons without any OVOCs (Peng and Jimenez, 2020). This is exactly the case for our experiments, but its influences on our conclusion were tiny, as have been discussed in the Section 3.1. ~~and the lower ratio of OH:HO₂ in our experiments than that in the ambient atmosphere was confirmed by a photochemical model in our previous study (Wang et al., 2020). In addition, high concentrations of radicals might also terminate the RO₂ chain earlier, which inhibits the autoxidation reactions in the PAM OFR.~~ Therefore, the difference in the distribution of products will not change our conclusion.~~However, these could only influence the distribution of oxidation products at most, and would not affect the chemical behaviors of HOMs under different OH exposures.~~

Such an active secondary OH chemistry is consistent with the fast OH reaction rates of HOMs. We take $C_{18}H_{26}O_8$ whose plausible structure is shown in Figure S4 as an example, which is the accretion product of two $C_9H_{13}O_5\cdot$. Its OH reaction rate constant is estimated to be around 2.07×10^{-10} cm^3 $molecule^{-1}$ s^{-1} according to the structure-activity relationship (Jenkin et al., 2018b, a), whose details are provided in Supplementary Text S2. This rate is several times larger than that of 1,3,5-TMB, which enables a very active secondary OH chemistry in the system. MCM recommended an OH reaction rate of 1.28×10^{-10} cm^3 $molecule^{-1}$ s^{-1} for TM135BPOOH ($C_9H_{14}O_5$) and 1.00×10^{-10} cm^3 $molecule^{-1}$ s^{-1} for TM135OBPOH ($C_9H_{12}O_4$) (Jenkin et al., 2003). The OH reaction rate for $C_{18}H_{26}O_8$ should also be fast due to the C=C bonds in its structure, which is activated by the adjacent functionalities. ~~The OH reaction rate for C₁₈H₂₆O₈ should be around twice of these values, as there are two C=C bonds in its structure.~~ Our calculation result is consistent with this estimation.

The distributions of C18 organonitrates also verified the extensive secondary reactions. The most abundant C18 organonitrate, $C_{18}H_{27}NO_{12}$ was a NO termination product of radical $C_{18}H_{27}O_{11}\cdot$, which, as mentioned above, was the radical generated from the OH reaction with $C_{18}H_{26}O_8$. $C_{18}H_{27}NO_{12}$ can also be formed either by accretion between a $C_9H_{15}O_m\cdot$ radical and a $C_9H_{12}NO_m\cdot$ radical or accretion between a $C_9H_{13}O_m\cdot$ radical and a $C_9H_{14}NO_m\cdot$ radical. Both $C_9H_{15}O_m\cdot$ and $C_9H_{14}NO_m\cdot$ radicals are a typical multi-generation RO_2 and thus prove $C_{18}H_{27}NO_{12}$ is a multi-generation OH oxidation product. Other C18 organonitrates are believed to be formed in a similar pathway. Hence, plenty of organonitrates have been formed via the multi-generation OH reactions of first-generation stabilized products.

Scheme 2 shows the NO termination pathways of the main BPR C$_9$H$_{13}$O$_5$• and its autoxidation product, C$_9$H$_{13}$O$_7$•. After introducing N$_2$O into PAM OFR, quantities of organonitrates were generated, including both C9 and C18 organonitrates. The averaged mass spectrometry of nitrate CIMS in the 1.8 ppb NO experiment and 4.8 ppb NO experiment is shown in Figure S4. Organonitrates were formed via the NO + RO$_2$ reaction, called as NO termination reactions. The distribution of oxidation products under these two NO settings were similar.

As discussed above, most of the first-generation HOMs should contain a C=C bond in the carbon backbone. The ubiquitous existence of organonitrates that contain two nitrogen atoms exactly confirms the extensive secondary OH oxidation in the systems, because the NO termination reaction of RO$_2$ is the only pathway that can generate organonitrates and this pathway can only introduce one nitrogen atom at a time, as indicated in Scheme 2. Taking the most abundant organonitrate, C$_9$H$_{14}$N$_2$O$_{10}$, as an example, it was exactly the NO termination product of C$_9$H$_{14}$NO$_9$•, which was generated from an OH attack and a subsequent O$_2$ addition to C$_9$H$_{13}$NO$_6$, the NO termination product of C$_9$H$_{13}$O$_5$•. For other organonitrates, C$_9$H$_{13}$NO$_8$, the second most abundant organonitrate, could be either a NO termination product of C$_9$H$_{13}$O$_7$• or, together with other most abundant organonitrates, C$_9$H$_{15}$NO$_7$ and C$_9$H$_{15}$NO$_8$, classical termination products of C$_9$H$_{14}$NO$_9$•.

The distributions of C18 organonitrates also verified the extensive secondary reactions. The most abundant C18 organonitrate, C$_{18}$H$_{27}$NO$_{12}$ was a NO termination product of radical C$_{18}$H$_{27}$O$_{11}$•, which, as mentioned above, was the radical generated from the OH reaction with C$_{18}$H$_{26}$O$_8$. Other C18 organonitrates are believed to be formed in a similar pathway since no evidence supports that a nitrogen-containing monomeric RO$_2$ can go through accretion reactions. Hence, plenty of organonitrates have been formed via the multi-generation OH reactions of first-generation stabilized products.

4 Atmospheric Implications

This study highlights the influences of OH exposure on the distribution and evolution of 1,3,5-TMB-derived HOMs. Secondary OH reactions can influence HOMs' composition by directly reacting with the stabilized first-generation oxidation products, leading to enhanced formation of HOMs. Organonitrates generated in the NO experiments further confirmed this. Due to the elevated abundance and the reduced volatility of HOMs, growth rates of newly formed nanoparticles in the presence of HOMs should be raised, especially in high-OH environments, which prevails in the summer noon. Substantially high concentrations of OH

710 have been frequently observed in polluted environments during summer, e.g., megacities in
711 China (Tan et al., 2019), and thus more active secondary OH reactions are expected compared
712 to wintertime. As a plausible consequence, seasonal differences of HOMs and new particle
713 formation (NPF) are resulted (Qiao et al., 2021; Yao et al., 2018; Guo et al., 2022). Furthermore,
714 previous studies suggest that high concentrations of NO can suppress the formation of HOMs
715 via the suppression of autoxidation (Pye et al., 2019), but the influences of such a suppression
716 could have been overestimated, since secondary OH reactions can continue to oxidize the
717 stabilized organonitrates. Our conclusions help to explain the existing gap between model
718 prediction and ambient measurement on the HOMs concentrations (Qi et al., 2018), and to build
719 a global HOMs simulation model.

720

721 *Data availability.* Data used in this work are available upon request from the corresponding
722 authors.

723

724 *Supplement.* The supplement related to this article is available online.

725

726 *Author contributions.* LW and Yuwei Wang designed the experiments. Yuwei Wang conducted
727 the laboratory experiments. Yuwei Wang analyzed the data. Yuwei Wang and LW wrote the
728 paper. All co-authors discussed the results and commented on the manuscript.

729

730 *Competing interests.* The authors declare that they have no conflict of interest.

731

732 *Acknowledgments.* This work was financially supported by the National Natural Science
733 Foundation of China (21925601, 22127811). The authors declare no competing interests.

References

Berndt, T., Mentler, B., Scholz, W., Fischer, L., Herrmann, H., Kulmala, M., and Hansel, A.: Accretion Product Formation from Ozonolysis and OH Radical Reaction of α-Pinene: Mechanistic Insight and the Influence of Isoprene and Ethylene, Environ. Sci. Technol., 52, 11069–11077, https://doi.org/10.1021/acs.est.8b02210, 2018a.

Berndt, T., Scholz, W., Mentler, B., Fischer, L., Herrmann, H., Kulmala, M., and Hansel, A.: Accretion Product Formation from Self- and Cross-Reactions of RO2 Radicals in the Atmosphere, Angew. Chemie - Int. Ed., 57, 3820–3824, https://doi.org/10.1002/anie.201710989, 2018b.

Bianchi, F., Kurtén, T., Riva, M., Mohr, C., Rissanen, M. P., Roldin, P., Berndt, T., Crounse, J. D., Wennberg, P. O., Mentel, T. F., Wildt, J., Junninen, H., Jokinen, T., Kulmala, M., Worsnop, D. R., Thornton, J. A., Donahue, N., Kjaergaard, H. G., and Ehn, M.: Highly Oxygenated Organic Molecules (HOM) from Gas-Phase Autoxidation Involving Peroxy Radicals: A Key Contributor to Atmospheric Aerosol, Chem. Rev., 119, 3472–3509, https://doi.org/10.1021/acs.chemrev.8b00395, 2019.

Cheng, X., Chen, Q., Li, Y. J., Zheng, Y., Liao, K., and Huang, G.: Highly Oxygenated Organic Molecules Produced by the Oxidation of Benzene and Toluene in a Wide Range of OH Exposure and NOx Conditions, Atmos. Chem. Phys., 1–23, https://doi.org/10.5194/acp-2021-201, 2021.

Crounse, J. D., Nielsen, L. B., Jørgensen, S., Kjaergaard, H. G., and Wennberg, P. O.: Autoxidation of organic compounds in the atmosphere, J. Phys. Chem. Lett., 4, 3513–3520, https://doi.org/10.1021/jz4019207, 2013.

Ehn, M., Thornton, J. A., Kleist, E., Sipilä, M., Junninen, H., Pullinen, I., Springer, M., Rubach, F., Tillmann, R., Lee, B., Lopez-Hilfiker, F., Andres, S., Acir, I. H., Rissanen, M., Jokinen, T., Schobesberger, S., Kangasluoma, J., Kontkanen, J., Nieminen, T., Kurtén, T., Nielsen, L. B., Jørgensen, S., Kjaergaard, H. G., Canagaratna, M., Maso, M. D., Berndt, T., Petäjä, T., Wahner, A., Kerminen, V. M., Kulmala, M., Worsnop, D. R., Wildt, J., and Mentel, T. F.: A large source of low-volatility secondary organic aerosol, Nature, 506, 476–479, https://doi.org/10.1038/nature13032, 2014.

Eisele, F. L. and Tanner, D. J.: Measurement of the gas phase concentration of H 2 SO 4 and methane sulfonic acid and estimates of H 2 SO 4 production and loss in the atmosphere, J. Geophys. Res. Atmos., 98, 9001–9010, https://doi.org/10.1029/93JD00031, 1993.

Garmash, O., Rissanen, M. P., Pullinen, I., Schmitt, S., Kausiala, O., Tillmann, R., Zhao, D., Percival, C., Bannan, T. J., Priestley, M., Hallquist, Å. M., Kleist, E., Kiendler-Scharr, A., Hallquist, M., Berndt, T., McFiggans, G., Wildt, J., Mentel, T. F., and Ehn, M.: Multi-generation OH oxidation as a source for highly oxygenated organic molecules from aromatics, Atmos. Chem. Phys., 20, 515–537, https://doi.org/10.5194/acp-20-515-2020, 2020.

Guo, Y., Yan, C., Liu, Y., Qiao, X., Zheng, F., Zhang, Y., Zhou, Y., Li, C., Fan, X., Lin, Z., Feng, Z., Zhang, Y., Zheng, P., Tian, L., Nie, W., Wang, Z., Huang, D., Daellenbach, K. R., Yao, L., Dada, L., Bianchi, F., Jiang, J., Liu, Y., Kerminen, V. M., and Kulmala, M.: Seasonal variation in oxygenated organic molecules in urban Beijing and their

776   contribution to secondary organic aerosol, Atmos. Chem. Phys., 22, 10077–10097,

777   https://doi.org/10.5194/acp-22-10077-2022, 2022.

778 Heinritzi, M., Simon, M., Steiner, G., Wagner, A. C., Kürten, A., Hansel, A., and Curtius, J.:

779   Characterization of the mass-dependent transmission efficiency of a CIMS, Atmos.

780   Meas. Tech., 9, 1449–1460, https://doi.org/10.5194/amt-9-1449-2016, 2016.

781 Hyttinen, N., Kupiainen-Määttä, O., Rissanen, M. P., Muuronen, M., Ehn, M., and Kurtén, T.:

782   Modeling the Charging of Highly Oxidized Cyclohexene Ozonolysis Products Using

783   Nitrate-Based Chemical Ionization, J. Phys. Chem. A, 119, 6339–6345,

784   https://doi.org/10.1021/acs.jpca.5b01818, 2015.

785 Iyer, S., Kumar, A., Savolainen, A., Barua, S., Daub, C., Pichelstorfer, L., Roldin, P.,

786   Garmash, O., Seal, P., Kurtén, T., and Rissanen, M.: Molecular rearrangement of

787   bicyclic peroxy radicals is a key route to aerosol from aromatics, Nat. Commun., 14,

788   4984, https://doi.org/10.1038/s41467-023-40675-2, 2023.

789 Jacob, D. J.: Introduction to atmospheric chemistry, Princeton, 1999.

790 Jenkin, M. E., Saunders, S. M., Wagner, V., and Pilling, M. J.: Protocol for the development

791   of the Master Chemical Mechanism, MCM v3 (Part B): tropospheric degradation of

792   aromatic volatile organic compounds, Atmos. Chem. Phys., 3, 181–193,

793   https://doi.org/10.5194/acp-3-181-2003, 2003.

794 Jenkin, M. E., Valorso, R., Aumont, B., Rickard, A. R., and Wallington, T. J.: Estimation of

795   rate coefficients and branching ratios for gas-phase reactions of OH with aliphatic

796   organic compounds for use in automated mechanism construction, 9297–9328 pp.,

797   https://doi.org/10.5194/acp-18-9297-2018, 2018a.

798 Jenkin, M. E., Valorso, R., Aumont, B., Rickard, A. R., and Wallington, T. J.: Estimation of

799   rate coefficients and branching ratios for gas-phase reactions of OH with aromatic

800   organic compounds for use in automated mechanism construction, Atmos. Chem. Phys.,

801   18, 9329–9349, https://doi.org/10.5194/acp-18-9329-2018, 2018b.

802 Keller-Rudek, H., Moortgat, G. K., Sander, R., and Sörensen, R.: The MPI-Mainz UV/VIS

803   spectral atlas of gaseous molecules of atmospheric interest, Earth Syst. Sci. Data, 5, 365–

804   373, https://doi.org/10.5194/essd-5-365-2013, 2013.

805 Krechmer, J., Lopez-Hilfiker, F., Koss, A., Hutterli, M., Stoermer, C., Deming, B., Kimmel,

806   J., Warneke, C., Holzinger, R., Jayne, J., Worsnop, D., Fuhrer, K., Gonin, M., and De

807   Gouw, J.: Evaluation of a New Reagent-Ion Source and Focusing Ion− Molecule Reactor

808   for Use in Proton-Transfer-Reaction Mass Spectrometry, Anal. Chem., 90, 12011–

809   12018, https://doi.org/10.1021/acs.analchem.8b02641, 2018.

810 Lambe, A., Massoli, P., Zhang, X., Canagaratna, M., Nowak, J., Daube, C., Yan, C., Nie, W.,

811   Onasch, T., Jayne, J., Kolb, C., Davidovits, P., Worsnop, D., and Brune, W.: Controlled

812   nitric oxide production via O(1D) + N2O reactions for use in oxidation flow reactor

813   studies, Atmos. Meas. Tech., 10, 2283–2298, https://doi.org/10.5194/amt-10-2283-2017,

814   2017.

815 Lambe, A., Krechmer, J., Peng, Z., Casar, J., Carrasquillo, A., Raff, J., Jimenez, J., and

816   Worsnop, D.: HO x and NO x production in oxidation flow reactors via photolysis of, 1–

817   22, 2018.

818 Lambe, A. T., Ahern, A. T., Williams, L. R., Slowik, J. G., Wong, J. P. S., Abbatt, J. P. D.,

819   Brune, W. H., Ng, N. L., Wright, J. P., Croasdale, D. R., Worsnop, D. R., Davidovits, P.,

and Onasch, T. B.: Characterization of aerosol photooxidation flow reactors: heterogeneous oxidation, secondary organic aerosol formation and cloud condensation nuclei activity measurements, Atmos. Meas. Tech, 4, 445–461, https://doi.org/10.5194/amt-4-445-2011, 2011.

Lambe, A. T., Chhabra, P. S., Onasch, T. B., Brune, W. H., Hunter, J. F., Kroll, J. H., Cummings, M. J., Brogan, J. F., Parmar, Y., Worsnop, D. R., Kolb, C. E., and Davidovits, P.: Effect of oxidant concentration, exposure time, and seed particles on secondary organic aerosol chemical composition and yield, Atmos. Chem. Phys., 15, 3063–3075, https://doi.org/10.5194/acp-15-3063-2015, 2015.

Lehtipalo, K., Yan, C., Dada, L., Bianchi, F., Xiao, M., Wagner, R., Stolzenburg, D., Ahonen, L. R., Amorim, A., Baccarini, A., Bauer, P. S., Baumgartner, B., Bergen, A., Bernhammer, A. K., Breitenlechner, M., Brilke, S., Buchholz, A., Mazon, S. B., Chen, D., Chen, X., Dias, A., Dommen, J., Draper, D. C., Duplissy, J., Ehn, M., Finkenzeller, H., Fischer, L., Frege, C., Fuchs, C., Garmash, O., Gordon, H., Hakala, J., He, X., Heikkinen, L., Heinritzi, M., Helm, J. C., Hofbauer, V., Hoyle, C. R., Jokinen, T., Kangasluoma, J., Kerminen, V. M., Kim, C., Kirkby, J., Kontkanen, J., Kürten, A., Lawler, M. J., Mai, H., Mathot, S., Mauldin, R. L., Molteni, U., Nichman, L., Nie, W., Nieminen, T., Ojdanic, A., Onnela, A., Passananti, M., Petäjä, T., Piel, F., Pospisilova, V., Quéléver, L. L. J., Rissanen, M. P., Rose, C., Sarnela, N., Schallhart, S., Schuchmann, S., Sengupta, K., Simon, M., Sipilä, M., Tauber, C., Tomé, A., Tröstl, J., Väisänen, O., Vogel, A. L., Volkamer, R., Wagner, A. C., Wang, M., Weitz, L., Wimmer, D., Ye, P., Ylisirniö, A., Zha, Q., Carslaw, K. S., Curtius, J., Donahue, N. M., Flagan, R. C., Hansel, A., Riipinen, I., Virtanen, A., Winkler, P. M., Baltensperger, U., Kulmala, M., and Worsnop, D. R.: Multicomponent new particle formation from sulfuric acid, ammonia, and biogenic vapors, Sci. Adv., 4, 1–10, https://doi.org/10.1126/sciadv.aau5363, 2018.

Li, R., Palm, B. B., Ortega, A. M., Hlywiak, J., Hu, W., Peng, Z., Day, D. A., Knote, C., Brune, W. H., De Gouw, J. A., and Jimenez, J. L.: Modeling the radical chemistry in an oxidation flow reactor: Radical formation and recycling, sensitivities, and the OH exposure estimation equation, J. Phys. Chem. A, 119, 4418–4432, https://doi.org/10.1021/jp509534k, 2015.

Lu, K. D., Rohrer, F., Holland, F., Fuchs, H., Bohn, B., Brauers, T., Chang, C. C., Häseler, R., Hu, M., Kita, K., Kondo, Y., Li, X., Lou, S. R., Nehr, S., Shao, M., Zeng, L. M., Wahner, A., Zhang, Y. H., and Hofzumahaus, A.: Observation and modelling of OH and HO2 concentrations in the Pearl River Delta 2006: A missing OH source in a VOC rich atmosphere, Atmos. Chem. Phys., 12, 1541–1569, https://doi.org/10.5194/acp-12-1541-2012, 2012.

Ma, X., Tan, Z., Lu, K., Yang, X., Chen, X., Wang, H., Chen, S., Fang, X., Li, S., Li, X., Liu, J., Liu, Y., Lou, S., Qiu, W., Wang, H., Zeng, L., and Zhang, Y.: OH and HO2 radical chemistry at a suburban site during the EXPLORE-YRD campaign in 2018, Atmos. Chem. Phys., 22, 7005–7028, https://doi.org/10.5194/acp-22-7005-2022, 2022.

Mehra, A., Wang, Y., E. Krechmer, J., Lambe, A., Majluf, F., A. Morris, M., Priestley, M., J. Bannan, T., J. Bryant, D., L. Pereira, K., F. Hamilton, J., R. Rickard, A., J. Newland, M., Stark, H., Croteau, P., T. Jayne, J., R. Worsnop, D., R. Canagaratna, M., Wang, L., and

864   Coe, H.: Evaluation of the chemical composition of gas- And particle-phase products of
865   aromatic oxidation, Atmos. Chem. Phys., 20, 9783–9803, https://doi.org/10.5194/acp-
866   20-9783-2020, 2020.

867 Mentel, T. F., Springer, M., Ehn, M., Kleist, E., Pullinen, I., Kurtén, T., Rissanen, M.,
868   Wahner, A., and Wildt, J.: Formation of highly oxidized multifunctional compounds:
869   Autoxidation of peroxy radicals formed in the ozonolysis of alkenes - Deduced from
870   structure-product relationships, Atmos. Chem. Phys., 15, 6745–6765,
871   https://doi.org/10.5194/acp-15-6745-2015, 2015.

872 Mohr, C., Thornton, J. A., Heitto, A., Lopez-hil, F. D., Lutz, A., Riipinen, I., Hong, J.,
873   Donahue, N. M., Hallquist, M., Petäjä, T., Kulmala, M., and Yli-juuti, T.: Molecular
874   identification of organic vapors driving atmospheric nanoparticle growth, Nat.
875   Commun., 1–7, https://doi.org/10.1038/s41467-019-12473-2, 2019.

876 Molteni, U., Bianchi, F., Klein, F., Haddad, I. El, Frege, C., Rossi, M. J., Dommen, J., and
877   Baltensperger, U.: Formation of highly oxygenated organic molecules from aromatic
878   compounds, Atmos. Chem. Phys, 18, 1909–1921, https://doi.org/10.5194/acp-18-1909-
879   2018, 2018.

880 Ng, N. L., Canagaratna, M. R., Zhang, Q., Jimenez, J. L., Tian, J., Ulbrich, I. M., Kroll, J. H.,
881   Docherty, K. S., Chhabra, P. S., Bahreini, R., Murphy, S. M., Seinfeld, J. H.,
882   Hildebrandt, L., Donahue, N. M., Decarlo, P. F., Lanz, V. A., Prévôt, A. S. H., Dinar, E.,
883   Rudich, Y., and Worsnop, D. R.: Organic aerosol components observed in Northern
884   Hemispheric datasets from Aerosol Mass Spectrometry, Atmos. Chem. Phys., 10, 4625–
885   4641, https://doi.org/10.5194/acp-10-4625-2010, 2010.

886 Orlando, J. J. and Tyndall, G. S.: Laboratory studies of organic peroxy radical chemistry: An
887   overview with emphasis on recent issues of atmospheric significance, Chem. Soc. Rev.,
888   41, 6294–6317, https://doi.org/10.1039/c2cs35166h, 2012.

889 Otkjær, R. V., Jakobsen, H. H., Tram, C. M., and Kjaergaard, H. G.: Calculated Hydrogen
890   Shift Rate Constants in Substituted Alkyl Peroxy Radicals, J. Phys. Chem. A, 122, 8665–
891   8673, https://doi.org/10.1021/acs.jpca.8b06223, 2018.

892 Peng, Z. and Jimenez, J. L.: Radical chemistry in oxidation flow reactors for atmospheric
893   chemistry research, Chem. Soc. Rev., 49, 2570–2616,
894   https://doi.org/10.1039/c9cs00766k, 2020.

895 Peng, Z., Day, D. A., Ortega, A. M., Palm, B. B., Hu, W., Stark, H., Li, R., Tsigaridis, K.,
896   Brune, W. H., and Jimenez, J. L.: Non-OH chemistry in oxidation flow reactors for the
897   study of atmospheric chemistry systematically examined by modeling, Atmos. Chem.
898   Phys., 16, 4283–4305, https://doi.org/10.5194/acp-16-4283-2016, 2016.

899 Pye, H. O. T., D'Ambro, E. L., Lee, B. H., Schobesberger, S., Takeuchi, M., Zhao, Y., Lopez-
900   Hilfiker, F., Liu, J., Shilling, J. E., Xing, J., Mathur, R., Middlebrook, A. M., Liao, J.,
901   Welti, A., Graus, M., Warneke, C., de Gouw, J. A., Holloway, J. S., Ryerson, T. B.,
902   Pollack, I. B., and Thornton, J. A.: Anthropogenic enhancements to production of highly
903   oxygenated molecules from autoxidation, Proc. Natl. Acad. Sci. U. S. A., 116, 6641–
904   6646, https://doi.org/10.1073/pnas.1810774116, 2019.

905 Qi, X., Ding, A., Roldin, P., Xu, Z., Zhou, P., Sarnela, N., Nie, W., Huang, X., Rusanen, A.,
906   Ehn, M., Rissanen, M. P., Petäjä, T., Kulmala, M., and Boy, M.: Modelling studies of
907   HOMs and their contributions to new particle formation and growth: comparison of

908   boreal forest in Finland and a polluted environment in China, Atmos. Chem. Phys, 18,
909   11779–11791, https://doi.org/10.5194/acp-18-11779-2018, 2018.

910 Qiao, X., Yan, C., Li, X., Guo, Y., Yin, R., Deng, C., Li, C., Nie, W., Wang, M., Cai, R.,
911   Huang, D., Wang, Z., Yao, L., Worsnop, D. R., Bianchi, F., Liu, Y., Donahue, N. M.,
912   Kulmala, M., and Jiang, J.: Contribution of Atmospheric Oxygenated Organic
913   Compounds to Particle Growth in an Urban Environment, Environ. Sci. Technol.,
914   https://doi.org/10.1021/acs.est.1c02095, 2021.

915 Qu, H., Wang, Y., Zhang, R., Liu, X., Huey, L. G., Sjostedt, S., Zeng, L., Lu, K., Wu, Y.,
916   Shao, M., Hu, M., Tan, Z., Fuchs, H., Broch, S., Wahner, A., Zhu, T., and Zhang, Y.:
917   Chemical Production of Oxygenated Volatile Organic Compounds Strongly Enhances
918   Boundary-Layer Oxidation Chemistry and Ozone Production, Environ. Sci. Technol., 55,
919   13718–13727, https://doi.org/10.1021/acs.est.1c04489, 2021.

920 Riva, M., Rantala, P., Krechmer, J. E., Peräkylä, O., Zhang, Y., Heikkinen, L., Garmash, O.,
921   Yan, C., Kulmala, M., Worsnop, D., and Ehn, M.: Evaluating the performance of five
922   different chemical ionization techniques for detecting gaseous oxygenated organic
923   species, Atmos. Meas. Tech, 12, 2403–2421, https://doi.org/10.5194/amt-12-2403-2019,
924   2019.

925 Slater, E. J., Whalley, L. K., Woodward-Massey, R., Ye, C., Lee, J. D., Squires, F., Hopkins,
926   J. R., Dunmore, R. E., Shaw, M., Hamilton, J. F., Lewis, A. C., Crilley, L. R., Kramer,
927   L., Bloss, W., Vu, T., Sun, Y., Xu, W., Yue, S., Ren, L., Acton, W. J. F., Hewitt, C. N.,
928   Wang, X., Fu, P., and Heard, D. E.: Elevated levels of OH observed in haze events
929   during wintertime in central Beijing, Atmos. Chem. Phys., 20, 14847–14871,
930   https://doi.org/10.5194/acp-20-14847-2020, 2020.

931 Stolzenburg, D., Fischer, L., Vogel, A. L., Heinritzi, M., Schervish, M., Simon, M., Wagner,
932   A. C., Dada, L., Ahonen, L. R., Amorim, A., Baccarini, A., Bauer, P. S., Baumgartner,
933   B., Bergen, A., Bianchi, F., Breitenlechner, M., Brilke, S., Mazon, S. B., Chen, D., Dias,
934   A., Draper, D. C., Duplissy, J., Haddad, I. El, Finkenzeller, H., Frege, C., Fuchs, C.,
935   Garmash, O., Gordon, H., He, X., Helm, J., Hofbauer, V., Hoyle, C. R., Kim, C., Kirkby,
936   J., Kontkanen, J., Kürten, A., Lampilahti, J., Lawler, M., Lehtipalo, K., Leiminger, M.,
937   Mai, H., Mathot, S., Mentler, B., Molteni, U., Nie, W., Nieminen, T., Nowak, J. B.,
938   Ojdanic, A., Onnela, A., Passananti, M., Petäjä, T., Quéléver, L. L. J., Rissanen, M. P.,
939   Sarnela, N., Schallhart, S., Tauber, C., Tomé, A., Wagner, R., Wang, M., Weitz, L.,
940   Wimmer, D., Xiao, M., Yan, C., Ye, P., Zha, Q., Baltensperger, U., Curtius, J.,
941   Dommen, J., Flagan, R. C., Kulmala, M., Smith, J. N., Worsnop, D. R., Hansel, A.,
942   Donahue, N. M., and Winkler, P. M.: Rapid growth of organic aerosol nanoparticles over
943   a wide tropospheric temperature range, Proc. Natl. Acad. Sci. U. S. A., 115, 9122–9127,
944   https://doi.org/10.1073/pnas.1807604115, 2018.

945 Tan, Z., Lu, K., Jiang, M., Su, R., Wang, H., Lou, S., Fu, Q., Zhai, C., Tan, Q., Yue, D.,
946   Chen, D., Wang, Z., Xie, S., Zeng, L., and Zhang, Y.: Daytime atmospheric oxidation
947   capacity in four Chinese megacities during the photochemically polluted season: A case
948   study based on box model simulation, Atmos. Chem. Phys., 19, 3493–3513,
949   https://doi.org/10.5194/acp-19-3493-2019, 2019.

950 Tröstl, J., Chuang, W. K., Gordon, H., Heinritzi, M., Yan, C., Molteni, U., Ahlm, L., Frege,
951   C., Bianchi, F., Wagner, R., Simon, M., Lehtipalo, K., Williamson, C., Craven, J. S.,

Duplissy, J., Adamov, A., Almeida, J., Bernhammer, A. K., Breitenlechner, M., Brilke, S., Dias, A., Ehrhart, S., Flagan, R. C., Franchin, A., Fuchs, C., Guida, R., Gysel, M., Hansel, A., Hoyle, C. R., Jokinen, T., Junninen, H., Kangasluoma, J., Keskinen, H., Kim, J., Krapf, M., Kürten, A., Laaksonen, A., Lawler, M., Leiminger, M., Mathot, S., Möhler, O., Nieminen, T., Onnela, A., Petäjä, T., Piel, F. M., Miettinen, P., Rissanen, M. P., Rondo, L., Sarnela, N., Schobesberger, S., Sengupta, K., Sipilä, M., Smith, J. N., Steiner, G., Tomè, A., Virtanen, A., Wagner, A. C., Weingartner, E., Wimmer, D., Winkler, P. M., Ye, P., Carslaw, K. S., Curtius, J., Dommen, J., Kirkby, J., Kulmala, M., Riipinen, I., Worsnop, D. R., Donahue, N. M., and Baltensperger, U.: The role of low-volatility organic compounds in initial particle growth in the atmosphere, Nature, 533, 527–531, https://doi.org/10.1038/nature18271, 2016.

Tsiligiannis, E., Hammes, J., Salvador, C. M., Mentel, T. F., and Hallquist, M.: Effect of NOx on 1,3,5-trimethylbenzene (TMB) oxidation product distribution and particle formation, Atmos. Chem. Phys., 19, 15073–15086, https://doi.org/10.5194/acp-19-15073-2019, 2019.

Vereecken, L.: Reaction Mechanisms for the Atmospheric Oxidation of Monocyclic Aromatic Compounds, Adv. Atmos. Chem., 377–527, https://doi.org/10.1142/9789813271838_0006, 2019.

Wang, S., Wu, R., Berndt, T., Ehn, M., and Wang, L.: Formation of Highly Oxidized Radicals and Multifunctional Products from the Atmospheric Oxidation of Alkylbenzenes, Environ. Sci. Technol., 51, 8442–8449, https://doi.org/10.1021/acs.est.7b02374, 2017.

Wang, W., Yuan, B., Peng, Y., Su, H., Cheng, Y., and Yang, S.: Direct observations indicate photodegradable oxygenated VOCs as larger contributors to radicals and ozone production in the atmosphere, Atmos. Chem. Phys., 1–28, 2022.

Wang, Y., Mehra, A., Krechmer, J. E., Yang, G., Hu, X., Lu, Y., Lambe, A., Canagaratna, M., Chen, J., Worsnop, D., Coe, H., and Wang, L.: Oxygenated products formed from OH-initiated reactions of trimethylbenzene: autoxidation and accretion, Atmos. Chem. Phys., 20, 9563–9579, https://doi.org/10.5194/acp-20-9563-2020, 2020.

Xu, L., Møller, K. H., Crounse, J. D., Kjaergaard, H. G., and Wennberg, P. O.: New insights into the radical chemistry and product distribution in the OH-initiated oxidation of benzene, Environ. Sci. Technol., 54, 13467–13477, https://doi.org/10.1021/acs.est.0c04780, 2020.

Yao, L., Garmash, O., Bianchi, F., Zheng, J., Yan, C., Kontkanen, J., Junninen, H., Mazon, S. B., Ehn, M., Paasonen, P., Sipilä, M., Wang, M., Wang, X., Xiao, S., Chen, H., Lu, Y., Zhang, B., Wang, D., Fu, Q., Geng, F., Li, L., Wang, H., Qiao, L., Yang, X., Chen, J., Kerminen, V.-M., Petäjä, T., Worsnop, D. R., Kulmala, M., and Wang, L.: Atmospheric new particle formation from sulfuric acid and amines in a Chinese megacity, Science (80-.)., 361, 278–281, https://doi.org/10.1126/science.aao4839, 2018.

Yuan, B., Chen, W., Shao, M., Wang, M., Lu, S., Wang, B., Liu, Y., Chang, C. C., and Wang, B.: Measurements of ambient hydrocarbons and carbonyls in the Pearl River Delta (PRD), China, Atmos. Res., 116, 93–104, https://doi.org/10.1016/j.atmosres.2012.03.006, 2012.

Zaytsev, A., Koss, A. R., Breitenlechner, M., Krechmer, J. E., Nihill, K. J., Lim, C. Y., Rowe, J. C., Cox, J. L., Moss, J., Roscioli, J. R., Canagaratna, M. R., Worsnop, D. R., Kroll, J.

996   H., and Keutsch, F. N.: Mechanistic study of the formation of ring-retaining and ring-
997   opening products from the oxidation of aromatic compounds under urban atmospheric
998   conditions, Atmos. Chem. Phys., 19, 15117–15129, https://doi.org/10.5194/acp-19-
999   15117-2019, 2019.

1000  Zhao, Y., Thornton, J. A., and Pye, H. O. T.: Quantitative constraints on autoxidation and
1001   dimer formation from direct probing of monoterpene-derived peroxy radical chemistry,
1002   Proc. Natl. Acad. Sci., 115, 12142–12147, https://doi.org/10.1073/pnas.1812147115,
1003   2018.

1004

Figure Captions

Figure 1. Normalized signals of HOM monomers and HOM dimers measured at the exit of OFR in experiments without NOx as a function of OH exposure. The solid lines represent fitting results using a gamma function to guide the eye.

Figure 2. Normalized signals of (a) $C_9H_{14}O_7$, $C_9H_{16}O_7$, and $C_9H_{16}O_8$ and (b) $C_9H_{14}O_8$, $C_9H_{16}O_8$, and $C_9H_{16}O_9$ measured at the exit of OFR in experiments without NO_x as a function of OH exposure. $C_9H_{16}O_8$ are shown in both plots to better illustrate the chemical profiles of different compound groups.

Figure 3. The nominal relative molar yield of HOM monomers containing (a) 12, (b) 14, and (c) 16 hydrogen atoms as a function of OH exposure in the OH-initiated 1,3,5-TMB oxidation experiments.

Figure 4. Normalized signals of (a) $C_{18}H_{26}O_{12}$, $C_{18}H_{28}O_{12}$, and $C_{18}H_{28}O_{13}$, and (b) $C_{18}H_{26}O_{10}$, $C_{18}H_{28}O_{10}$, and $C_{18}H_{28}O_{11}$ measured at the exit of OFR in experiments without NO_x as a function of OH exposure.

Figure 5. The nominal relative molar yield of (a) $C_{18}H_{26}O_{10}$ and $C_{18}H_{26}O_{12}$ and (b) $C_{18}H_{28}O_{10}$, $C_{18}H_{28}O_{12}$, and $C_{18}H_{28}O_{13}$ as a function of OH exposure in the OH-initiated 1,3,5-TMB oxidation experiments.
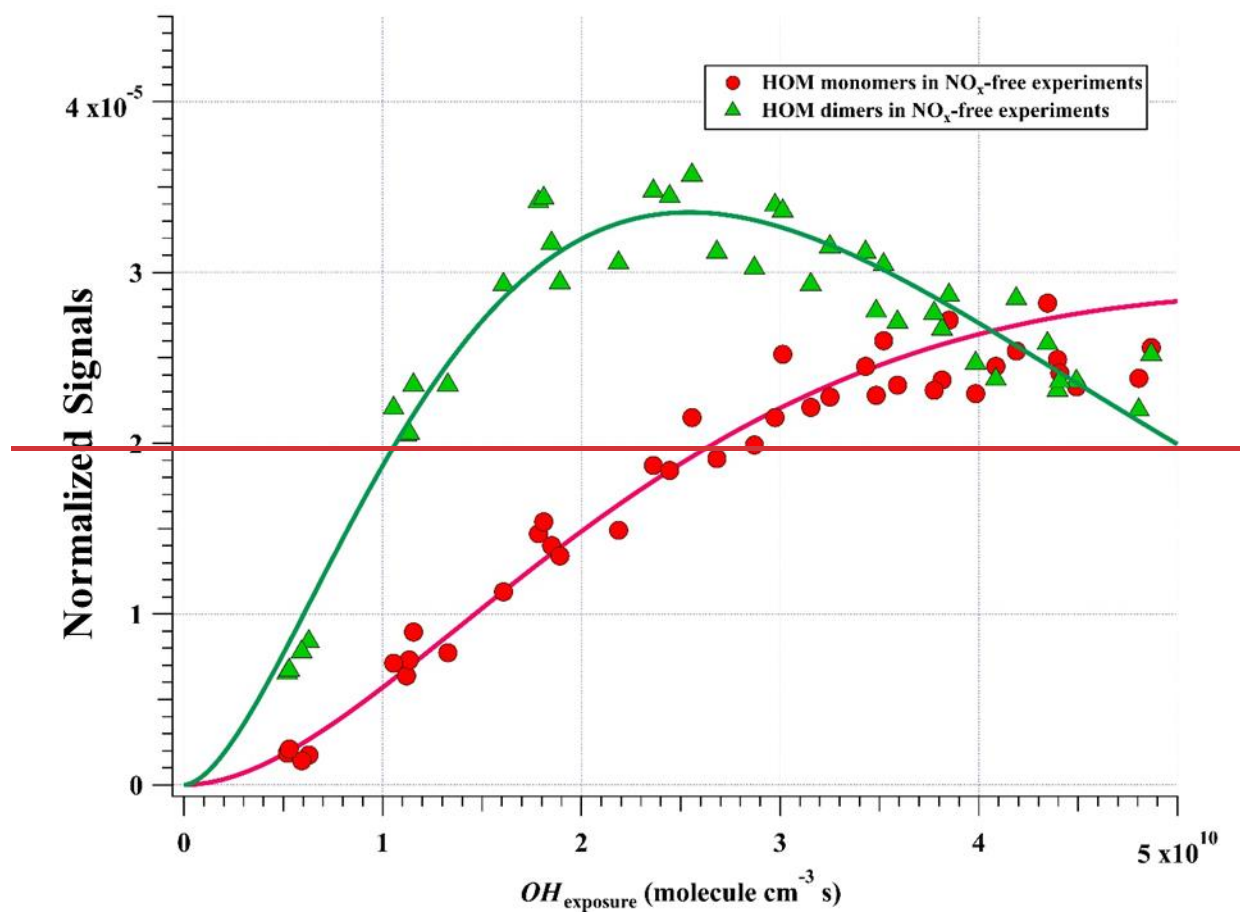
Figure 1
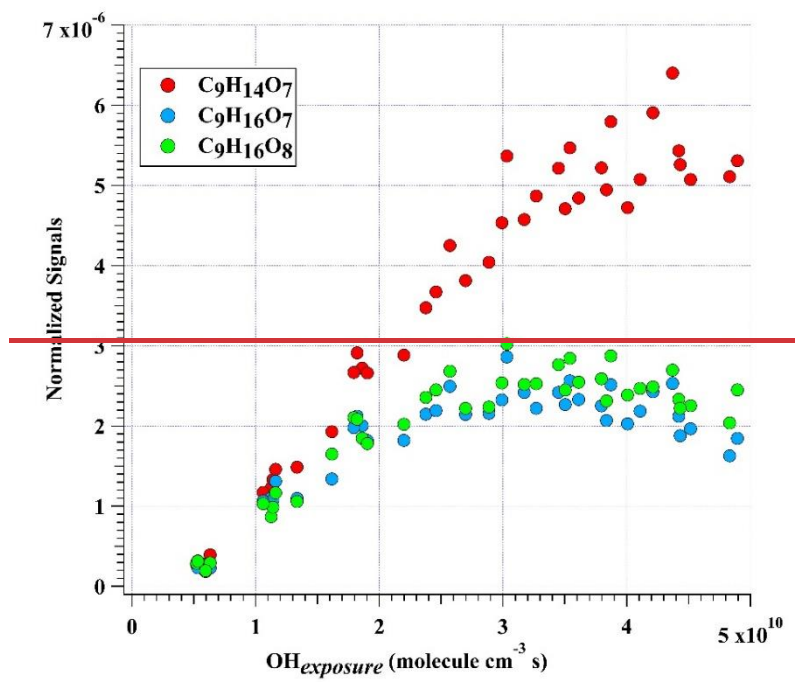
Figure 2a
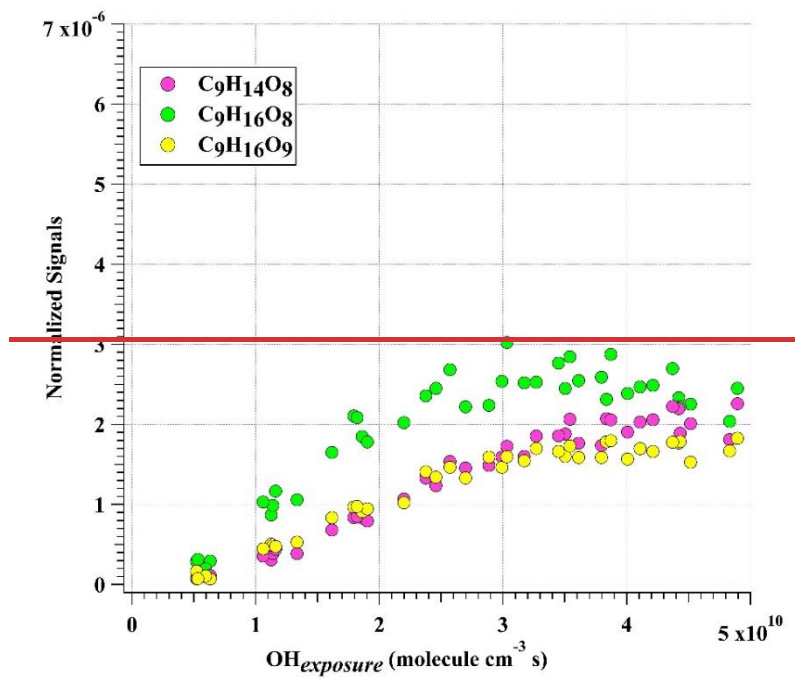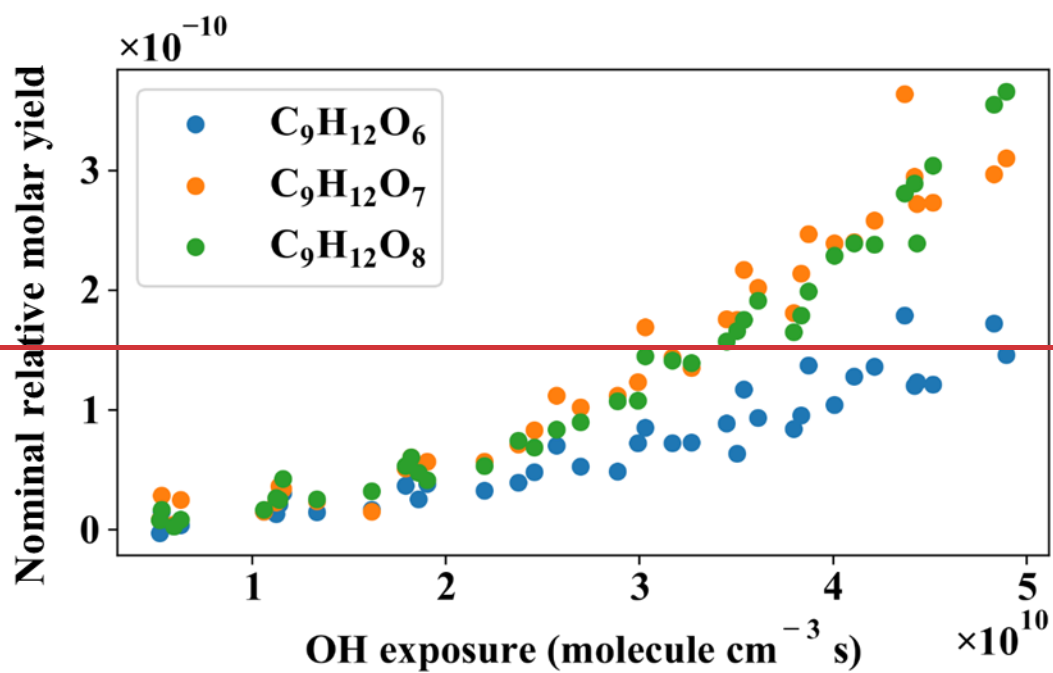
Figure 2b
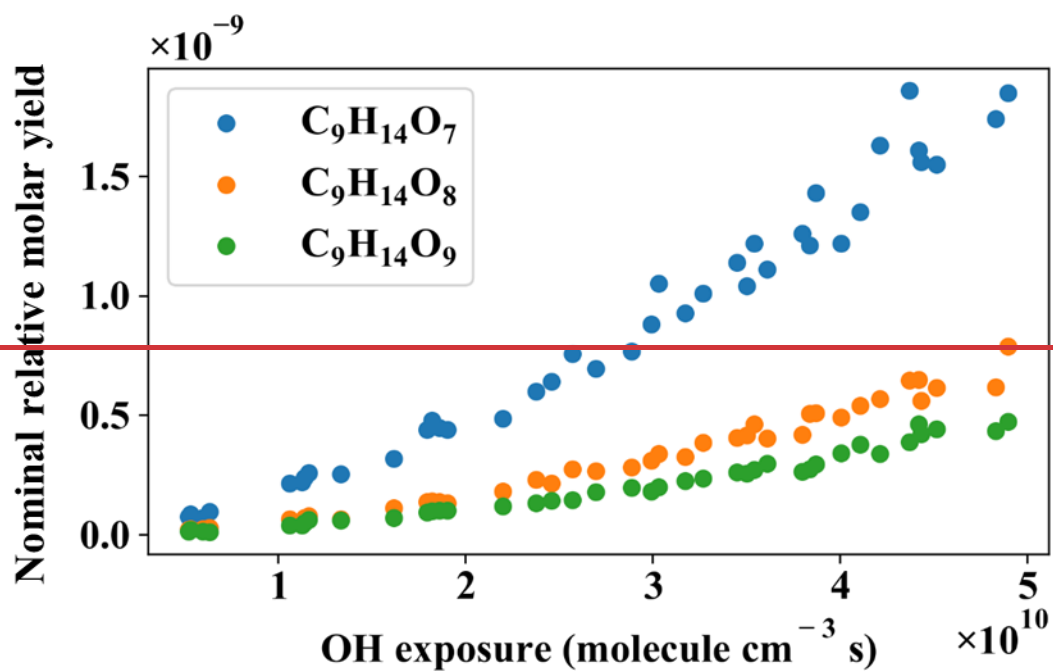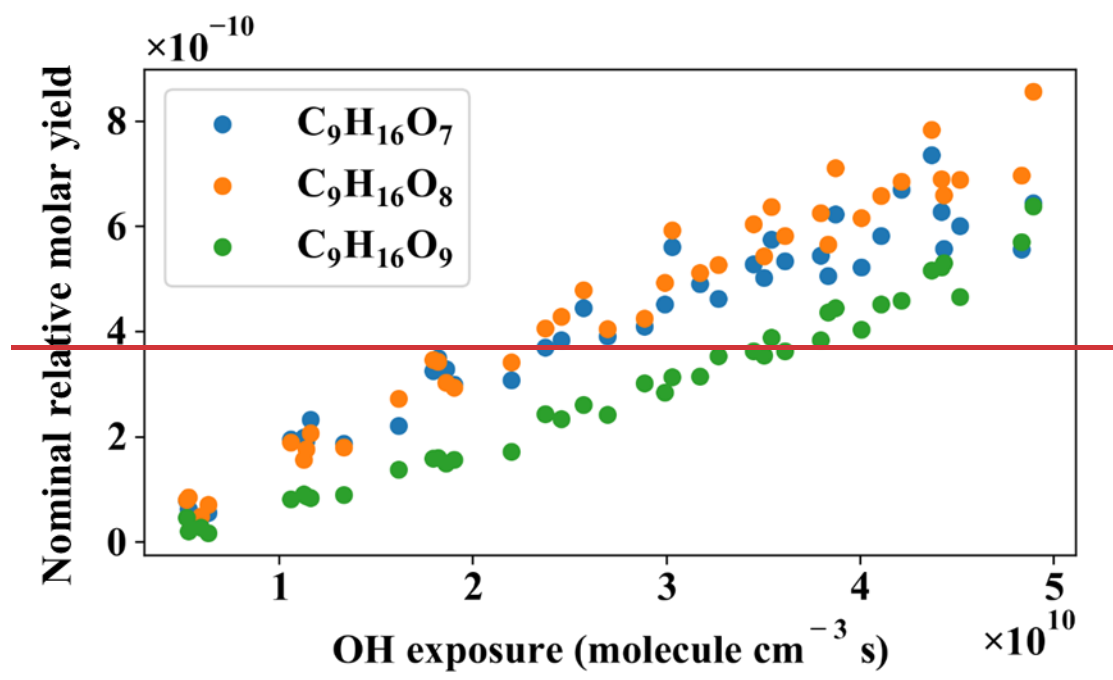
Figure 3e
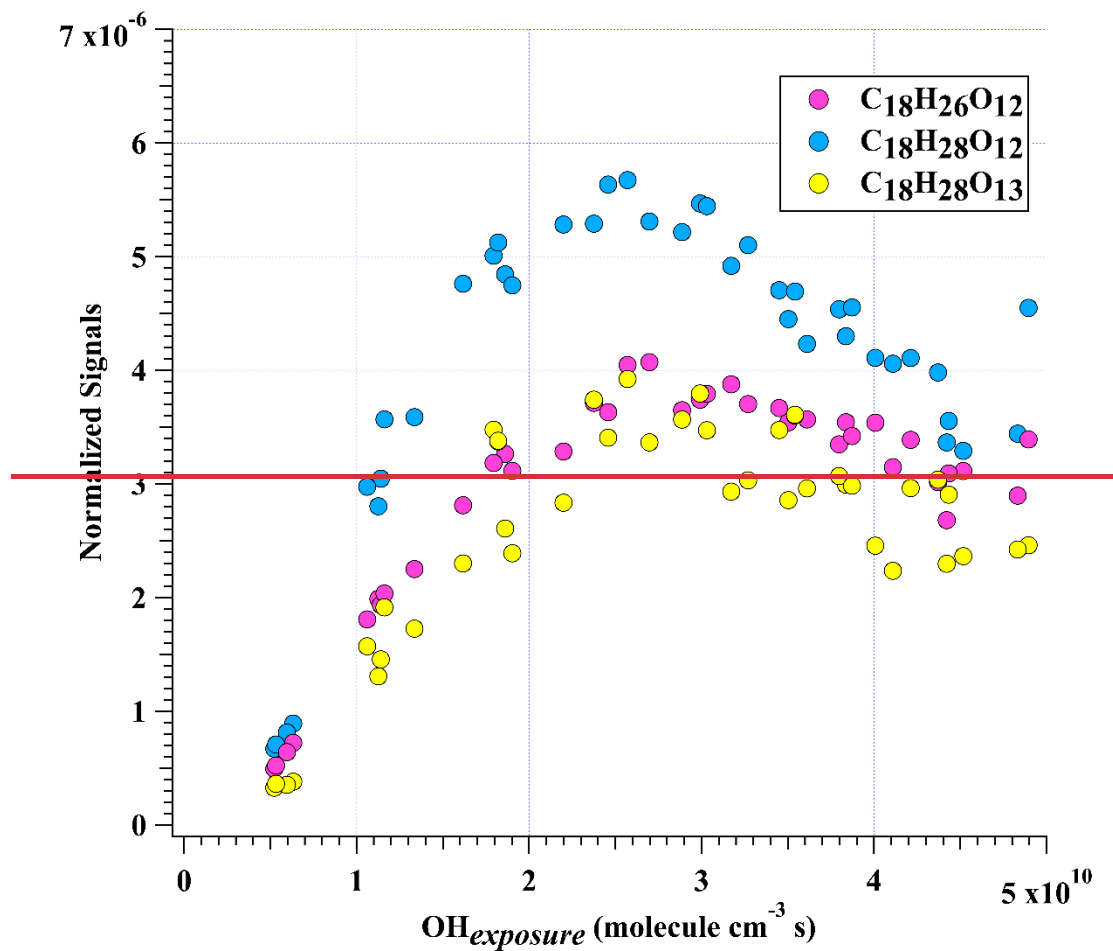
Figure 4a
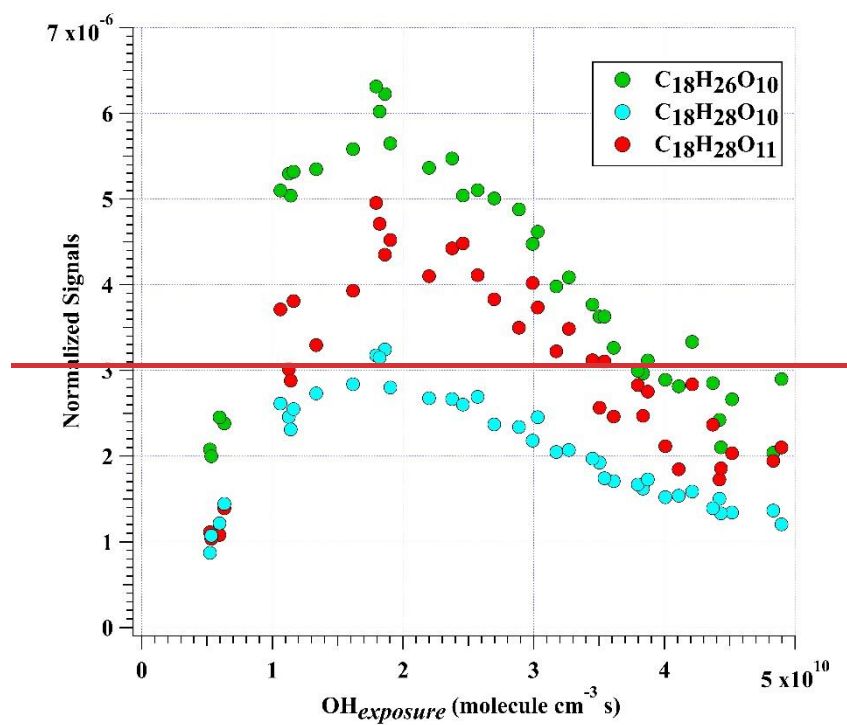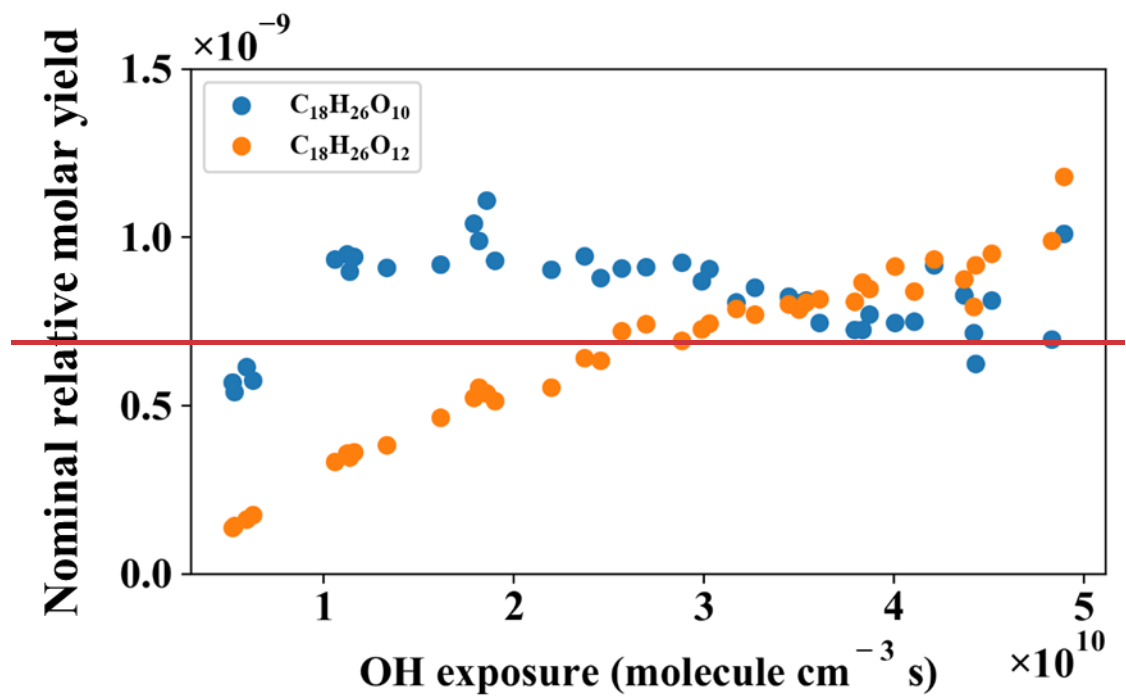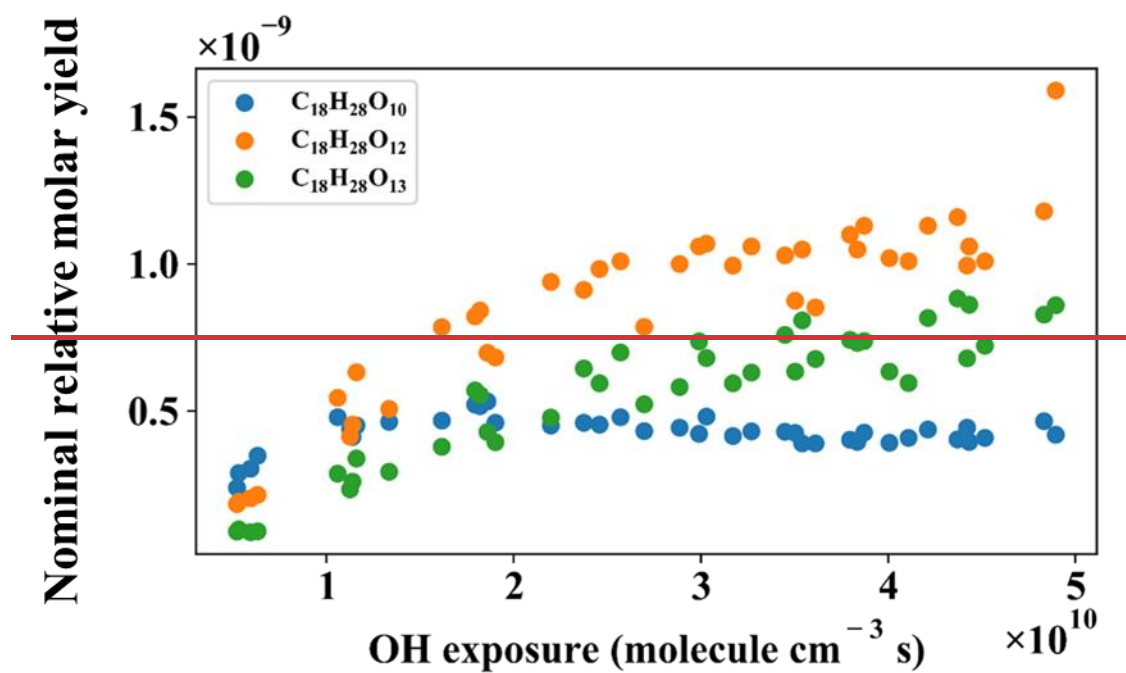
Figure 4b

Scheme Captions

Scheme 1. Oxidation pathways of the bicyclic peroxy radical $C_9H_{13}O_5\cdot$ (MCM name: TM135BPRO2) in the OH initiated oxidation of 1,3,5 TMB. Green, blue, and black formulae denote alkyl peroxy radicals, alkoxy radicals and stabilized products, respectively. Red arrows denote the autoxidation pathway. MCM names for $HO_2\cdot$ and RO_2 termination products of TM135BPRO2 are present, whereas MCM names for termination products of $C_9H_{13}O_7\cdot$ are unavailable and thus named according to the autoxidation intermediates.

Scheme 2. NO termination reactions of the bicyclic peroxy radical $C_9H_{13}O_5\cdot$ (MCM name: TM135BPRO2) and its autoxidation reaction products. Green, blue, and black formulae denote alkyl peroxy radicals, alkoxy radicals and stabilized products, respectively. Red arrows denote the autoxidation pathway. MCM names of NO termination products of TM135BPRO2 are present, whereas MCM names for termination products of $C_9H_{13}O_7\cdot$ are unavailable and thus named according to the autoxidation intermediates.

Scheme 1

Scheme 2